공학박사 학위논문

Synthesis of Carbon Supported Nanoparticles via Sputtering onto Liquids and their Electrocatalytic Applications

액체 기판 스퍼터링을 통한 담지 촉매 제작 및 전기화학 촉매로의 적용

2014년 8월

서울대학교 대학원

공과대학 화학생물공학부

차 인 영

Synthesis of Carbon Supported Nanoparticles via Sputtering onto Liquids and their Electrocatalytic Applications

지도 교수 성 영 은

이 논문을 공학박사 학위논문으로 제출함
2014년 7월

서울대학교 대학원
공과대학 화학생물공학부
차 인 영

차인영의 박사 학위논문을 인준함
2014년 7월

위 원 장 ____________________________ (인)

부위원장 ____________________________ (인)

위 원 ____________________________ (인)

위 원 ____________________________ (인)

위 원 ____________________________ (인)

Abstract

Synthesis of Carbon Supported Nanoparticles via Sputtering onto Liquids and their Electrocatalytic Applications

In Young Cha
School of Chemical and Biological Engineering
The Graduate School
Seoul National University

Evenly dispersed platinum nanoparticles on carbon supports have been intensively investigated as an electrochemical catalyst for various reactions, due to their intrinsic high catalytic activities and large surface to volume ratio. Chemical method, which uses reduction of metal precursors, is most widely applied procedure to synthesis carbon supported platinum nanoparticle. However, this method has environmentally and economically limitations due to price of metal precursors and use of reducing agents and surfactant.

This study aimed to develop new carbon supported platinum nanoparticle synthesis technique which minimizes the use of precursors, reducing agents and surfactants, and reveal their synthetic mechanism. Moreover, fabricated particles are applied as electrochemical catalyst; catalytic performance was evaluated via oxygen reduction reaction.

Direct sputtering method onto ionic liquid substrate was selected to synthesize well dispersed platinum nanoparticles. Platinum sputtering was directly conducted onto carbon supports containing ionic liquids and interaction between carbon supports and platinum nanoparticle was strengthened by post heat treatment. Carbon supported platinum nanoparticles were easily obtained, but synthesized particles were not suitable for electrochemical catalyst due to strong adsorption of anions in ionic liquid.

Non-volatile PEG substrate was applied as alternative and supported nanoparticles were successfully synthesized without post heat treatment. It was proved that liquid sputtering could be a promising method for synthesis supported nanoparticle, since fabricated particles exhibited significant catalytic performance.

This synthesis was not only limited to single platinum material, but also various structured multi-metal nanoparticles via modifying synthetic procedures.

PtCo/C and PtNi/C catalysts were prepared by co-sputtering, various analysis revealed alloy nanoparticle formation. Altered electronic structure and reduced atomic distance were detected using XRD, XAFS and XPS. Enhanced ORR activity was obtained due to above reasons and particularly PtNi/C had 2-fold catalytic activity than sing component Pt/C catalyst.

Core-shell structured nanoparticles were synthesized by microwave assisted two step liquid sputtering method. Core material was fabricated using normal liquid sputtering method and shell was deposited by microwave irradiation. Although synthesized particle has just average diameter of 2-3 nm, core-shell structure was formed. Synthesized particles exhibited superior catalytic activity due to electron transfer effect and lattice strain of core material.

Evenly dispersed magnetic oxide nanoparticles were also synthesized by injecting carbon supports after sputtering. Fabricated cobalt oxide nanoparticle was promising bi0functional catalyst since catalyst showed considerable ORR and OER activities.

Consequently, supported nanoparticles with various structures and compositions were easily synthesized via facile sputtering method, and achieved further enhanced catalytic activities.

Keywords: sputtering, ionic liquid, PEG, supported nano catalyst, oxygen reduction reaction

Student Number: 2009-21029

Contents

List of Tables

List of Figures

Chapter 1. Introduction

1. 1. Fuel cells and nanocatalyst

Fuel Cell is a device that converts chemical energy directly to electrical energy. In 1842, first fuel cell was demonstrated by William Robert Grove, who focused on hydrogen and oxygen production through electrolysis and devised reverse cell named gas voltaic battery.[1][2] The first fuel cell produced electrical energy by combining hydrogen and oxygen.

Fuel cell technology is based upon the simple combustion reaction by the following equations:

$H_2 \rightarrow 2H^+ + 2e^-$, $E^0 = 0.0$ V (anode)

$O_2 + 4e^- + 4H^+ \rightarrow 2H_2O$, $E^0 = 1.23$ V (cathode)

$H_2 + 1/2\ O_2 \rightarrow H_2O$, $\Delta E = 1.23$ V (combined reaction)

Generated electrons are collected through outer circuit to make electricity. In general, systems consist of porous electrodes and thin electrolyte membranes, such as figure 1.1 (reprinted from [3]), are utilized to increase interface between electrode and electrolyte. At the negative anode, a fuel typically hydrogen is being oxidized, while at the positive cathode, oxygen is reduced. Ions are transported through the electrolyte from one side to the other. The electrolyte determines the temperature window of operation, and types of fuel cells are determined by operation conditions.

1. Proton Exchange Membrane Fuel Cells (PEMFC), also called polymer electrolyte fuel cells, use acidic polymer membrane and platinum-based catalysts for both electrodes. Normally hydrogen fuel is supplied and protons are transported through membrane. Operation temperature is relatively low (20 – 80 ℃) and suitable for vehicles.

2. Phosphoric Acid Fuel Cells (PAFC) use liquid phosphoric acid in a bonded silicon carbide matrix as electrolyte and finely dispersed platinum catalysts on carbon as electrode. PAFS have slightly better resistant to carbon monoxide poisoning than PEMFC due to higher operating temperature (100 - 205 ℃), and used in stationary power generators (100 kW - 400 kW).

3. Alkaline Fuel Cells (AFC) use mobilized or immobilized potassium hydroxide electrolyte, so hydroxide ions act as charge carrier. Transition metal catalysts electrodes are applied and operation window is larger than PEMFC (40 - 220 ℃). External reformer is required, since AFC is very sensitive to carbon monoxide poisoning, likewise PEMFC.

4. Solid Oxide Fuel Cells (SOFC) are operated at very high temperature (400 – 1000 ℃), so generally perovskite electrodes are used, instead of precious metal catalyst. Oxygen anions are transported through solid ceramic electrolyte.

5. Molten Carbonate Fuel cells (MCFC) are also operated at very high temperature (600 – 800 ℃), nickel oxide electrode, instead of precious metal, is used. Electrolyte is a molten carbonate salt suspended in a porous ceramic, and carbonate ions act as charge carrier.

Fuel cells have tremendous benefits in various aspects. First of all, fuel cells emit low or zero greenhouse gas depends on fuel. Pure hydrogen fuel cell emits zero emissions, and some stationary fuel cells produce far fewer emissions than conventional power plants, although they use natural gas or hydrocarbons as a hydrogen feedstock (Greenhouse gas emissions are illustrated in figure 1.2, reprinted from [4]). Also fuel cells are much quieter than many incumbent technologies, since they use no combustion or moving parts (figure 1.3, reprinted from [4]). This allows fuel cells to be used in residential or built up areas where the noise pollution is undesirable. Moreover, no combustion means that fuel cells are not subjected to thermodynamic rules such as ‘Carnot limit’. Therefore, thermodynamic efficiency of a hydrogen fuel cell could be greater than 90%, while internal combustion engines have 10 – 20 % efficiency. [5]

One of the biggest problems of current fuel cell is low practical efficiency; state-of-the-art fuel cells for vehicles have efficiencies near 50%. Low efficiency is originated from high overpotential at cathode electrode. Overpotential for hydrogen oxidation at anode is only 50 mV, whereas oxygen reduction reaction, which breaks strong O-O bond (498 kJ/mol), at cathode has an overpotential of 500 – 600 mV even at platinum electrode. [5] Figure 1.4 (reprinted from [6]) shows the cell voltage decreases with increased current output. Due to the high overpotential of the oxygen reduction reaction, substantial current densities cannot be achieved at voltages even close to the thermodynamic value of 1.2 V. High catalysts loadings are required to achieve substantial current densities of desired magnitude. This leads significant increase of cost, and as part of effort to reduce cost, platinum nanoparticles supported onto porous carbon surfaces have been developed in order to increase catalytic utilization.

Nanoparticles have a large surface area to volume ratio and quantum effect to allow the particles to be more reactive than bulk materials. Proportion of surface atom depends on particle size; 50 % of atoms exist on surface for 3 nm sized particle, whereas only 5 % of atoms exist on surface of 30 nm sized particle. [7] Considering catalytic reactions occur on the surface of catalyst, it is clear that high ratio of surface atom directly associated with high activity. Moreover, it is well known that the performance of catalysts can be improved by uniformly dispersed nanoparticles on large surface area carbons. [8][9][10]

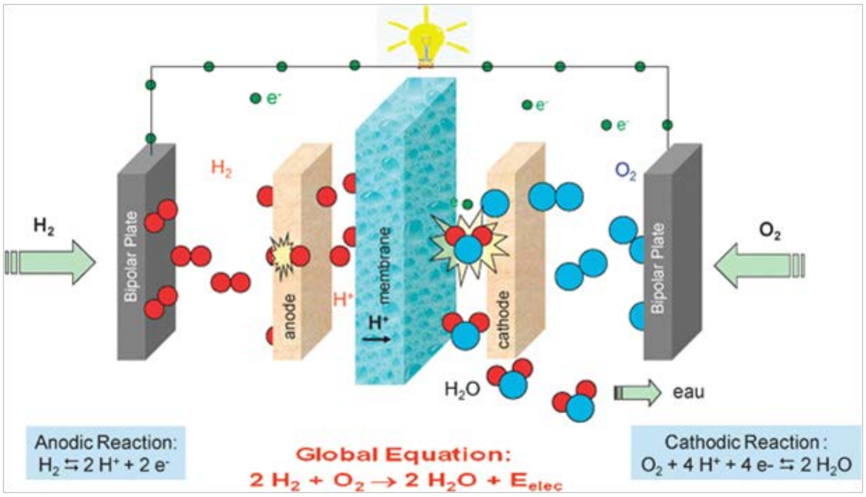

Figure 1. 1 Diagram of fuel cell

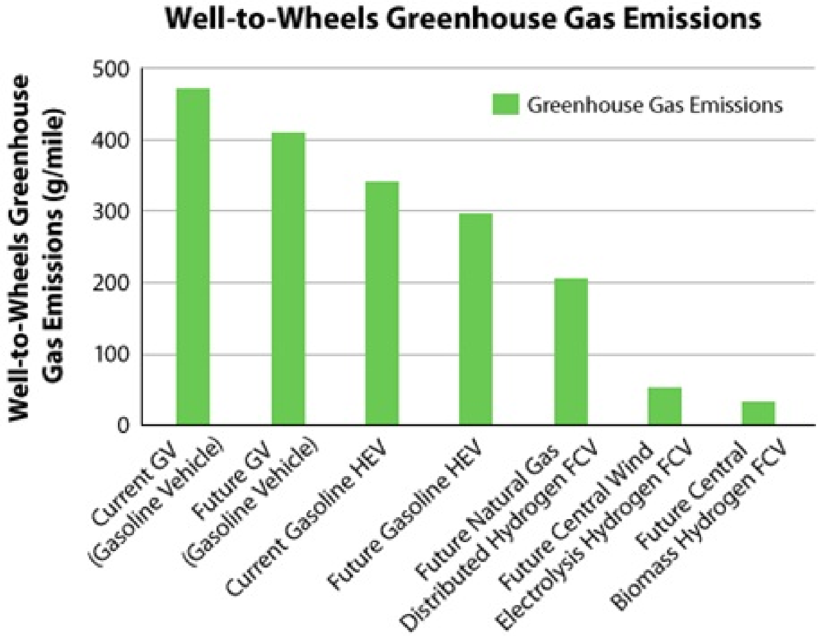

Figure 1. 2 Greenhouse gas emissions

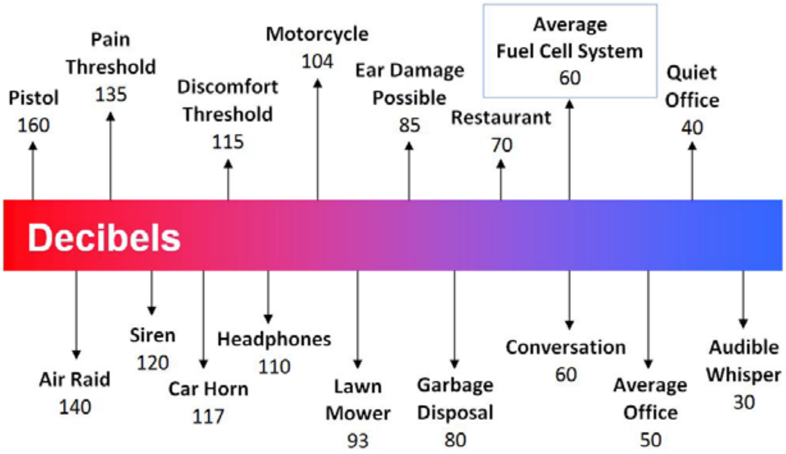

Figure 1. 3 Noise from fuel cell

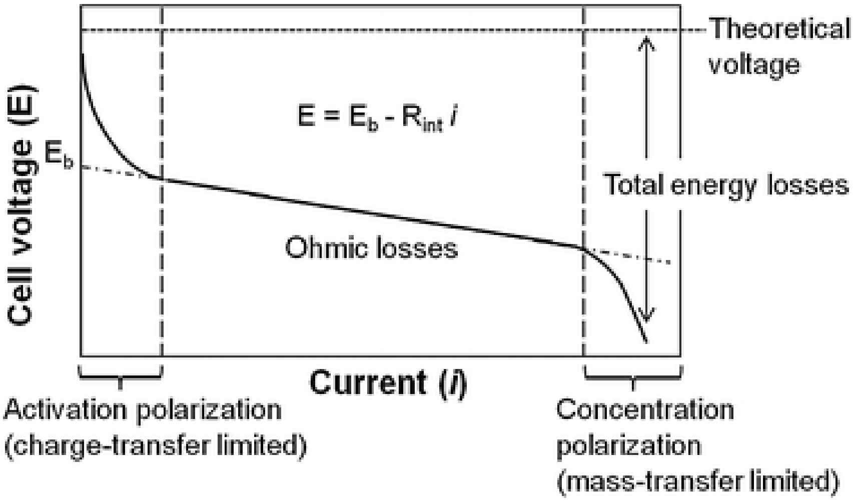

Figure 1. 4 Polarization curve of fuel cell and major overpotentials

1. 2. Basis of sputtering technique

Sputtering is an atom ejection process from solid target material due to bombardment of the target by energetic particles. [11] In 1852, sputtering phenomenon was first discovered by W. Grove who observed film deposition on the anode plated during tube discharge experiments using a silver needle cathode. By reversing the voltage, he also managed to sputter the deposit off again. Sputtering process can be applied to surface etching, analysis or film deposition using ejected atoms. Herein, sputtering coating technique will be described.

Sputtering technique is widely using for thin film coating, and it is a form of physical vapor deposition (PVD) likewise pulsed laser deposition (PLD) and e-beam evaporation. The principles of the sputtering are as follows. When a voltage is applied between anode and cathode, after injecting small amount of inert gas (normally argon) into vacuum chamber, electrons emitted from cathode collide with argon gas atoms to ionize the argon. Once plasma-the fourth state of matter, gas ionized into cations and electrons by applied higher energy than ionization energy, collective behavior, electrically neutral medium- is formed in this way, argon cations are accelerated toward cathode target surface and transfer energy to target atoms by bombardment. If transferred energy is larger than binding force between target atoms, atoms are ejected from target and deposited onto anode substrate. In order to effectively transfer energy, argon -inert gas with relatively large atomic weight- is most often used. Schematic structure of sputtering equipment is illustrated in figure 1.5 (reprinted from [12]).

Sputtering characteristics are determined by various factors. Applied potential (V) is closely related to sputtering rate. Sputtering rate is proportional to number of ejected atoms per incident ion (sputtering yield) and sputtering yield is affected by energy of incoming ions which is determined by voltage on cathode. Mean free path is another factor for determining sputtering efficiency and it is reverse proportional to working pressure. Too short mean free path, collision (bombardment) happens well but particles are scattered during movement, whereas too long, insufficient collision occurs. In case of argon atmosphere, maximum efficiency appears around 110 mT. Sputtering power also impact to thin film properties, poor microstructure with void is fabricated at low sputtering power since particles arriving to the substrate have inadequate energy for moving. [13] Film properties according to working pressure and substrate temperature are illustrated in figure 1.6 (reprinted from [14]), Thornton thin film structure zone model.

Sputtering is divided into two types, DC and RF, by power source. DC sputtering is basic sputtering equipment with fast film deposition rate and good uniformity, but limited to conducting target. When non conducting target is mounted to DC sputter, further ionization (plasma formation) is impossible and discharge is stopped, once cathode surface is charged with accelerated argon cations. In order to overcome this drawback, RF sputtering is developed.

Cathode surface is rapidly changes from negative to positive voltage by flowing AC current with 13.56 MHz, and accumulated argon cations are removed during positive voltage state. However, equipment is complicated and film formation rate is slow compared to DC device. In addition, magnetron sputtering with enhanced sputtering rate by magnet arranged behind the cathode and reactive sputtering for compound film formation are also present.

Sputtering technique has clean working condition, uniformity, reproducibility, good adhesion and advantageous in scale-up. Various structures such as porous, dense, columnar and coarse and various phase such as polycrystalline and amorphous can be fabricated by controlling conditions. Target materials are unlimited, so metal, alloy, compound, non conducting substance film are formed with RF sputtering. Despite these advantages, sputtering has not been widely applied to fuel cell since small surface area of thin film is not suitable for catalyst.

Less restriction on the choice of materials is one of the biggest advantages of sputtering compared to commonly used solution method. Solution method is strongly dependent on reduction potential of precursor because nanoparticles are prepared by reduction of organometallic compound solutions in the presence of surfactant molecules. Therefore, synthesis of early transition metals with extremely negative reduction potential is almost impossible. In contrast, sputtering which uses physical detachment is not governed by such constraints. Thus, sputtering technique is currently applied to fuel cells for screening and possibility ensuring of uncommon composition thin films. [15]

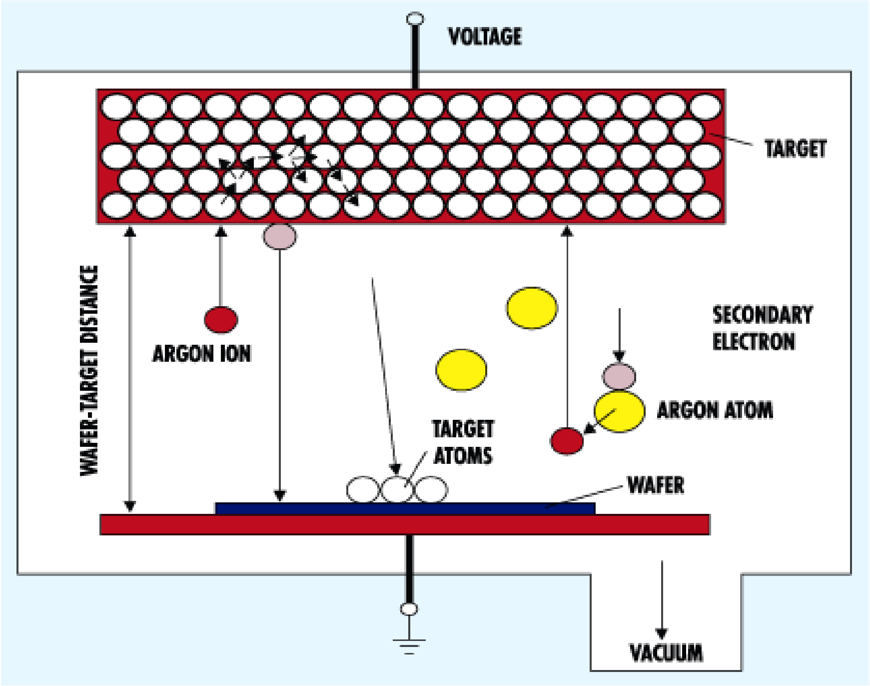

Figure 1. 5 Schematic diagram of sputter

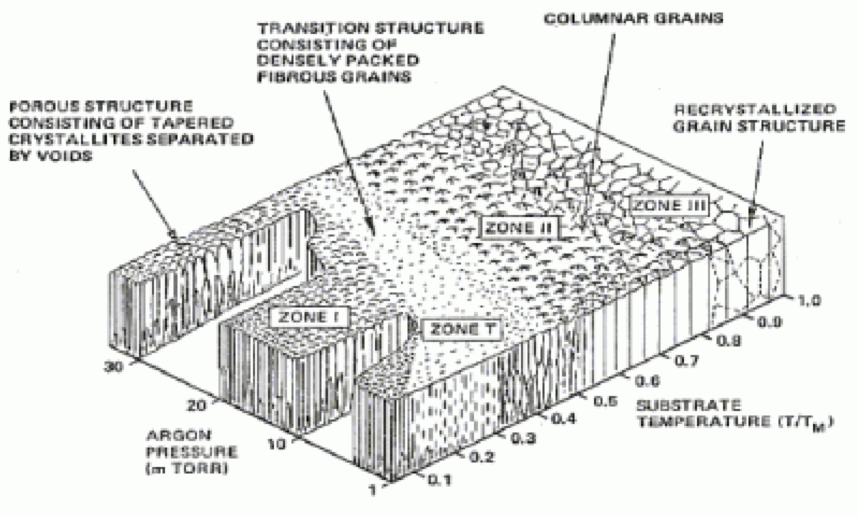

Figure 1. 6 Thornton thin film structure zone model

1. 3. Nanoparticle synthesis via sputtering technique

Recently, nanoparticle synthesis by sputtering has been reported. Sputtering was conducted on ionic liquid substrate and nano-sized metal particles were successfully produced in ionic liquid as colloidal solution state. Extremely low vapor pressure of ionic liquid allows such synthesis.

The origin of the liquid sputtering dates back to 1996. [16] The purposed direction was fairly different from now. The purpose was film deposition onto liquid surface, so silver film was sputter deposited onto silicon oil drop and several papers about film deposition on liquid were reported as a follow-up study. [17][18] In 1999, research for nanoparticle suspension via sputtering was developed for the first time. Iron was sputtered on mineral oil or silicon oil and magnetic suspension containing iron nanoparticles was obtained. [19]

In 2006, the first paper aiming for nanoparticle synthesis using liquid sputtering was published. [20] Colloidal gold nanoparticle was synthesized in two ionic liquids; N,N,N-trimethyl-N-propylammonium bis(trifluoromethanesulfonyl)imide (TMPA TFSI) and 1-ethyl-3-methylimidazolium tetrafluoroborate (EMI BF_4). Nanoparticles have 1.9 nm and 5.5 nm of diameter respective to TMPA TFSI and EMI BF_4. Types of ionic liquid affect to size of nanoparticles since they serve the role of stabilizer and matrix simultaneously. Silver [21], palladium [22], platinum [23], indium [24] and transition metal (W, Mo, Nb, Ti) nanoparticles [25] were synthesized under same technique and gold-platinum alloy nanoparticles

[23] were also fabricated using divided target. Liquid sputtering is theoretically possible for all vacuum stable liquids with low vapor pressure and sputtering onto castor oil [26] and poly ethylene glycol (PEG) [27] had been reported.

Growing mechanism of nanoparticles is not clearly reported, but it is presumed to follow one of three different scenarios depending on surface tension; (i) the atomic nucleation starts on the IL surface and then diffuses into the liquid phase, where particle growth takes place; (ii) both processes occur on the IL surface or (iii) the metal atoms and clusters penetrate to just below the liquid surface, and both processes occur in the bulk IL phase. Each assumption is illustrated in figure 1.7 (reprinted from [28]). [28] In addition, it has been reported that large particles are obtained in low viscosity liquid due to easy diffusion. Interaction between metal particle and ions in ionic liquid is determined by particle size; small particles tend to interact preferentially with anionic aggregates of the ILs, whereas large ones probably interact preferentially with the cationic aggregates (Figure 1.8, reprinted from [29]). [29]

Studies on synthesis and analysis of nanoparticles from liquid sputtering has been actively investigated, while research about collecting nanoparticles from liquid substrate or applying for catalyst is still lacking. Adsorbing particles on solid substrates (Si, HOPG) [30][31] or collecting particles through injecting additional surfactant are only reported. [32] Thus, there are many barriers to apply practical catalyst. Particle collecting technique without surfactant and without agglomeration is required and strongly adsorbed ions of ionic liquid should be removed even if surfactant is not used. Moreover, research on fabricate supported nanoparticle must be carried out in order to increase catalyst efficiency.

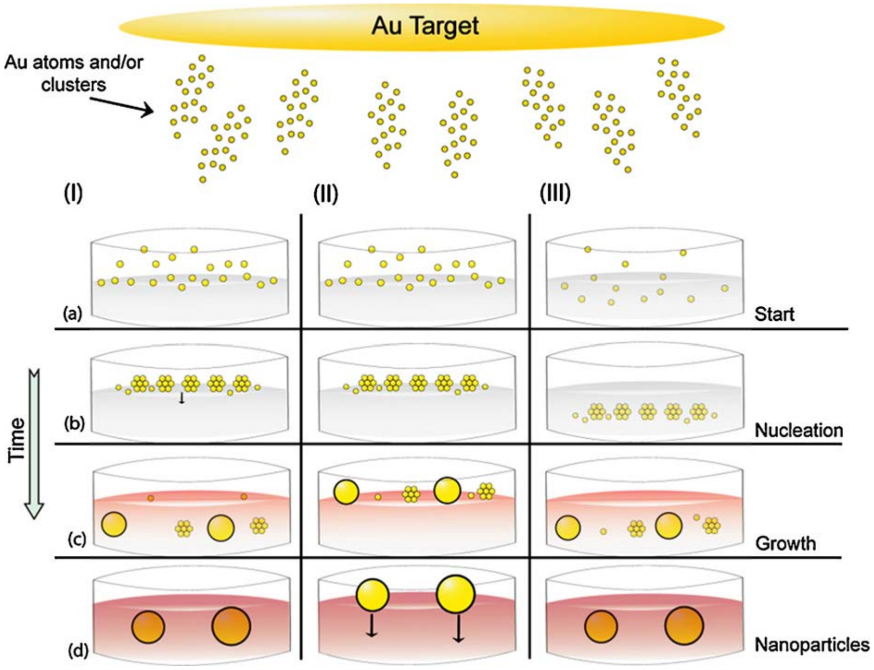

Figure 1. 7 Possible mechanisms for the nucleation and growth of sputtered gold nanoparticles into ILs

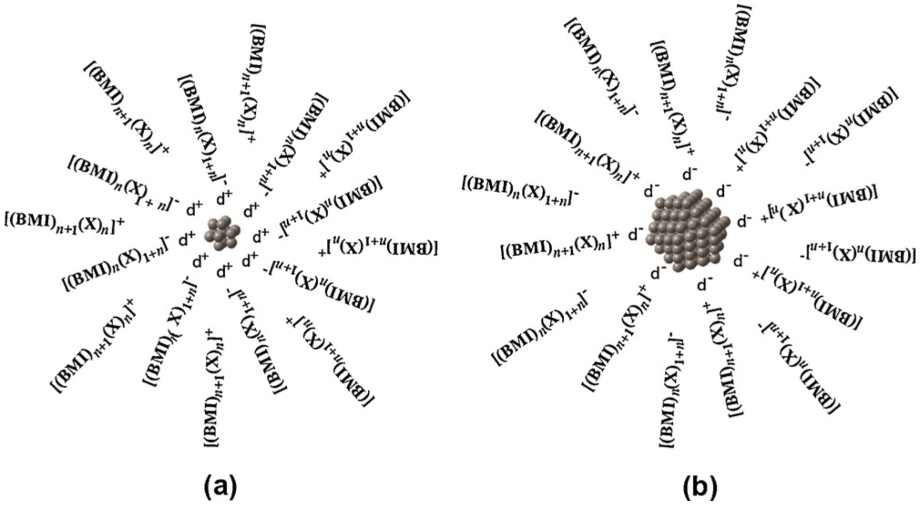

Figure 1. 8 Interaction of metal NPs with IL supramolecular aggregates: (a) small particles tend to interact preferentially with anionic aggregates of the ILs, whereas (b) large ones probably interact preferentially with the cationic aggregates.

1. 4. Subject of research in the thesis

This study aims to develop synthesis technique which has advantages of sputtering and supported nano-scale catalyst. In other words, the purpose is successful combination of advantages of sputtering – cost effective, reproducibility, easy scale up, continuous process and Etc.- and highly active large surface area nanomaterials on supports.

Despite of the aforementioned advantages, sputtering technique was limited to thin film coatings. However, basis on recently reported sputtering nanoparticle synthesis on non volatile liquids, we predicted supported nanoparticle synthesis via sputtering could be a new synthesis method. In this study, supports materials were applied during sputtering process in order to synthesize supported nanoparticle. Expansion of sputtering application range is also expected with this method.

Beyond the simple synthesis of supported nanoparticle, supporting conditions were intensively investigated to establish supporting mechanism. In this process, role of ions for supporting process was revealed. This mechanism study will suggest ionic liquid selection for further researches.

In addition to ionic liquids, cost effective and environmental friendly PEG solvent was also adopted to synthesize commercially applicable catalyst.

Uniform nanoparticles with very narrow size distribution were successfully synthesized via the proposed method, even though no additional surfactant was used. The proposed method is less affected by reduction potential of precursors and clean process is possible because of minimized precursor usage. Moreover, modified liquid sputtering syntheses are suggested to prepare alloy or core-shell structured nanoparticles; co-sputtering and microwave assisted liquid sputtering. Catalytic performances of synthesized single or multi component materials will be also evaluated.

1. 5. References

[1] W. R. Grove, On a new Voltaic Combination, The London and Edinburgh Philosophical Magazine and Journal of Science, 1838.

[2] W. R. Grove, On Voltaic Series and the Combination of Gases by Platinum, Philosophical Magazine and Journal of Science, 1839, 127-130.

[3] C. Laberty-Robert, K. Vallé, F. Pereira and C. Sanchez, “Design and properties of functional hybrid organic–inorganic membranes for fuel cells”, *Chem. Soc. Rev.*, **2011**, 40, 961–1005

[4] http://www.fuelcells.org/

[5] A. A. Gewirth and M. S. Thorum, "Electroreduction of Dioxygen for Fuel-Cell Applications: Materials and Challenges," *Inorg. Chem.*, **2010**, 49, 3557-3566.

[6] X. Dominguez-Benetton, S. Sevda, K. Vanbroekhoven and D. Panta, “The accurate use of impedance analysis for the study of microbial electrochemical systems”, *Chem. Soc. Rev.*, **2012**, 7, 7228-7246.

[7] N. Taniguchi, “On the Basic Concept of Nanotechnology”, Proc. Int. Conf. Prod. Eng. Tokyo, **1974**, 18.

[8] M. S. Wilson and S. Gottesfeld, “Thin-film catalyst layers for polymer electrolyte fuel cell electrodes”, *J. Appl. Electrochem.*, **1992**, 22, 1-7.

[9] Y. Liu, X. Chen, J. Li and C. Burda, “Photocatalytic degradation of azo dyes by nitrogen-doped TiO2 nanocatalysts”, *Chemosphere.*, **2005**, 61, 11-18.

[10] Z. Liu, L. M. Gan, L. Hong, W. Chen and J. Y. Lee, “Carbon-supported Pt nanoparticles as catalysts for proton exchange membrane fuel cells”, *J. Power Sources,* **2005**, 139, 73-78.

[11] R. Behrisch, Sputtering by Particle bombardment, Springer, 1981.

[12] http://micromagazine.fabtech.org/archive/02/07/rampf.html

[13] S. A. Pethe, E. Takahashi, A. Kaul and N. G. Dhere, “Effect of sputtering process parameters on film properties of molybdenum back contact”, *Sol. Energ. Mat. Sol. C.,* **2012**, 100, 1-5.

[14] J. A. Thornton, “Structure-Zone Models Of Thin Films”, Proc. SPIE, 1988, 821, 95.

[15] S. J. Yoo, K.-S. Lee, S. J. Hwang, Y.-H. Cho, S.-K. Kim, J. W. Yun, Y.-E. Sung and T.-H. Lim, “Pt3Y electrocatalyst for oxygen reduction reaction in proton exchange membrane fuel cells”, *Int. J. Hydrogen Energ.,* **2012**, 37, 9758-9765.

[16] G. X. Ye, Q. R. Zhang, C. M. Feng, H. L. Ge and Z. K. Jiao, “Structural and electrical properties of a metallic rough-thin-film system deposited on liquid substrates”, *Phys. Rev. B,* **1996**, 54, 14754-14757.

[17] H. L. Ge, C. M. Feng, G. X. Ye, Y. H. Ren and Z. K. Jiao, “Growth mechanism and electrical properties of metallic films deposited on silicone oil surfaces”, *J. Appl. Phys.,***1997**, 82, 5469-5471.

[18] J.-S. Jin, A.-G. Xia and G.-X. Ye, “Diffusion and aggregation behaviors of silver atoms on charged liquid substrates”, *Acta Phys. Sin.,* **2002**, 51, 2144-2149.

[19] M. Wagener and B. Günther, “Sputtering on liquids – a versatile process for the production of magnetic suspensions?”, *J. Magn. Magn. Mater.*, **1999**, 201, 41-44.

[20] T. Torimoto, K. Okazaki, T. Kiyama, K. Hirahara, N. Tanaka and S. Kuwabata, “Sputter deposition onto ionic liquids: Simple and clean synthesis of highly dispersed ultrafine metal nanoparticles”, *Appl. Phys. Lett.*, **2006**, 89, 243117.

[21] K. Okazaki, T. Kiyama, K. Hirahara, N. Tanaka, S. Kuwabata and T. Torimoto, “Single-step synthesis of gold–silver alloy nanoparticles in ionic liquids by a sputter deposition technique”, *Chem. Commun.*, **2008**, 691–693.

[22] M. Hirano, K. Enokida, K. Okazaki, S. Kuwabata, H. Yoshida and T. Torimoto, “Composition-dependent electrocatalytic activity of AuPd alloy nanoparticles prepared via simultaneous sputter deposition into an ionic liquid”, *Phys. Chem. Chem. Phys.*, **2013**, 15, 7286-7294.

[23] S. Suzuki, T. Suzuki, Y. Tomita, M. Hirano, K. Okazaki, S. Kuwabata and T. Torimoto, “Compositional control of AuPt nanoparticles synthesized in ionic liquids by the sputter deposition technique”, *CrystEngComm.*, **2012**, 14, 4922-4926.

[24] T. Suzuki, K. Okazaki, S. Suzuki, T. Shibayama, S. Kuwabata, and T. Torimoto, “Nanosize-Controlled Syntheses of Indium Metal Particles and Hollow Indium Oxide Particles via the Sputter Deposition Technique in Ionic Liquids”, *Chem. Mater.*, **2010**, 22, 5209–5215.

[25] T. Suzuki, S. Suzuki, Y. Tomita, K. Okazaki, T. Shibayama, S. Kuwabata and T. Torimoto, “Fabrication of Transition Metal Oxide Nanoparticles Highly Dispersed in Ionic Liquids by Sputter Deposition”, *Chem. Lett.,* **2010**, 39, 1072-1074.

[26] H. Wender, L. F. de Oliveira, A. F. Feil, E. Lissner, P. Migowski, M. R. Meneghetti, S. R. Teixeira and J. Dupont, “Synthesis of gold nanoparticles in a biocompatible fluid from sputtering deposition onto castor oil”, *Chem. Commun.,* **2010**, 46, 7019–7021.

[27] Y. Hatakeyama, T. Morita, S. Takahashi, K. Onishi and K. Nishikawa, “Synthesis of Gold Nanoparticles in Liquid Polyethylene Glycol by Sputter Deposition and Temperature Effects on their Size and Shape”, *J. Phys. Chem. C,* **2011**, 115, 3279-3285.

[28] H. Wender, L. F. de Oliveira, P. Migowski, A. F. Feil, E. Lissner, M. H. G. Prechtl, S. R. Teixeira and J. Dupont, “Ionic Liquid Surface Composition Controls the Size of Gold Nanoparticles Prepared by Sputtering Deposition”, *J. Phys. Chem. C,* **2010**, 114, 11764-11768.

[29] J. Dupont and J. D. Scholten, “On the structural and surface properties of transition-metal nanoparticles in ionic liquids”, *Chem. Soc. Rev.,* **2010**, 39, 1780-1804.

[30] O. P. Khatri, K. Adachi, K. Murase, K. Okazaki, T. Torimoto, N. Tanaka, S. Kuwabata and H. Sugimura, “Self-Assembly of Ionic Liquid (BMI-PF6)-Stabilized Gold Nanoparticles on a Silicon Surface: Chemical and Structural Aspects”, *Langmuir,* **2008**, 24, 7785–7792.

[31] K. Okazaki, T. Kiyama, T. Suzuki, S. Kuwabata and T. Torimoto, "Thermally Induced Self-assembly of Gold Nanoparticles Sputter-deposited in Ionic Liquids on Highly Ordered Pyrolytic Graphite Surfaces", *Chem. Lett.,* **2009**, 38, 330-331.

[32] D. Konig, K. Richter, A. Siegel, A.-V. Mudring and A. Ludwig, "High-Throughput Fabrication of Au–Cu Nanoparticle Libraries by Combinatorial Sputtering in Ionic Liquids", *Adv. Funct. Mater.,* **2014**, 24, 2049–2056.

Chapter 2. Experimental

2.1. Synthesis of carbon supported metal nanoparticle

2.1.1. Carbon supported Pt nanoparticles

1-Ethyl-3-methylimidazolium tetrafluoroborate (EMI BF_4, > 98 %), 1-propyl-3-methylimidazolium bis(trifluoromethylsulfonyl)imide (PMI TFSI, > 98 %) and 1-butyl-3-methylimidazolium bis(trifluoromethylsulfonyl)imide (BMI TFSI, > 98 %) were purchased from Sigma-Aldrich. 1-Ethyl-3-methylimidazolium bis(trifluoromethylsulfonyl)imide (EMI TFSI, > 98 %), 1-hexyl-3-methylimidazolium bis(trifluoromethylsulfonyl)imide (HMI TFSI, > 98 %) and trimethylpropylammonium bis(trifluoromethylsulfonyl)imide (TMPA TFSI, > 98 %) were received from TCI. N-propyl-N-methylpyrrolidinium bis(trifluoromethylsulfonyl)imide (PMPyrd TFSI), N-propyl-N-methylpyrrolidinium bis(fluorosulfonyl)imide (PMPyrd FSI) and N-propyl-N-methylpyrrolidinium tetrafluoroborate (PMPyrd BF_4) were obtained from Seoul national university fine chemical laboratory. Additional EMI FTSI and TMPA TFSI were also obtained from fine chemical laboratory for reconfirmation. Poly ethylene glycol (PEG) with average molecular weight of 600 and ethanol (95.0 %) for filtering were purchased from Sigma-Aldrich and samchun chemicals, respectively. Carbon black (Vulcan XC-72) was purchased from Carbot corporation. Deionized water was obtained through a Mili-Q system (millipore water, 18.2 MΩ•cm). Multiwall carbon nanotube (CNT) purchased from Carbon Nano-material Technology co. was used as extra support. CNT with 20 nm diameter and 5 µm length was acid treated with 1 M H_2SO_4 and 1M HNO_3 to introduce more functional groups. Nitric acid (HNO_3, 69.0 %) and sulfuric acid (H_2SO_4, 99.999 %) were purchased from Fluka and Sigma-Aldrich, respectively.

Carbon powders (20 mg) were dispersed in 20 mL of ionic liquids or PEG, and then carbon containing solvents were set into load lock chamber of sputtering system. Load lock chamber was maintained at a vacuum state for one hour to remove moisture or volatile impurities contained in liquids. When impurity removal is complete, carbon containing solvents were transferred to main chamber of sputtering system and sputtering was proceeded.

RF sputter deposition was performed with the KVS-2004 Sputtering System at a base pressure of 1×10^{-5} Torr and an Ar working pressure of 1×10^{-2} Torr. The sputtering system has 4 target guns in radial direction. Pure Pt (99.95 %) target was located 20 cm away from the liquid substrate with diagonal direction. Pt sputtering was conducted with a power of 300 W for 10 minutes, after 30 minutes pre-sputtering for target cleaning. When ionic liquids were applied as substrates, consecutive vacuum annealing process in the sputtering chamber was performed after sputtering in order to strengthen binding forces between NPs and supports.

Particles dispersed in solvents were collected by ethanol filtering. After filtering with ethanol, the samples were dried at 75°C for 5 hours. Then the samples were heat treated under air for 2 hours and continuously in reducing atmosphere for additional 2 hours at 160 °C to remove surface impurities.

2.1.2. Carbon supported Co_3O_4 nanoparticles

Ethylene glycol (anhydrous, 99.8 %) was purchased from Sigma-Aldrich. Nitrogen doped activated carbon named N2299 was received from Stan Lee and applied to additional support as well as untreated CNT.

Carbon supported Co_3O_4 nanoparticles were prepared by two different methods.

First, carbon powders (20 mg) were dispersed in 20 mL PEG, and then carbon containing PEG was set into load lock chamber of sputtering system. Load lock chamber was maintained at a vacuum state for one hour to remove moisture or volatile impurities contained in PEG. When impurity removal is complete, carbon containing PEG was transferred to main chamber and sputtering was proceeded. Pure Co (99.95 %) target was located 20 cm away from the liquid substrate. Co sputtering was conducted with a power of 300 W for 30 minutes, after 30 minutes pre-sputtering for target cleaning.

Particles dispersed in solvents were collected by ethanol filtering. After filtering with ethanol, the samples were dried at 75°C for 5 hours. Then the samples were heat treated under air for 2 hours at 250 °C to remove surface impurities and oxidize as prepared cobalt nanoparticles to cobalt oxide nanoparticles.

The second method for improving dispersion was introduced. PEG without carbon supports was set into load lock chamber of sputtering system and maintained in vacuum for one hour. When impurity removal is complete, PEG was transferred to main chamber and sputtering was proceeded in exactly same condition as the previous method.

Carbon supports (20 mg) were injected after dilution of cobalt nanoparticle containing PEG (20 mL) with 60 mL ethylene glycol. Carbon supports were dispersed in the solution through one hour sonication, and particles were supported on carbon trough overnight stirring. After overnight stirring, identical experimental process for filtering, drying and heat treatment were performed.

2.1.3. Carbon supported PtCo and PtNi alloy nanoparticles

PtCo alloy nanoparticles were prepared by Pt and Co co-sputtering.

Carbon powders (20 mg) were dispersed in 20 mL of ionic liquids or PEG, and then carbon containing solvents were set into load lock chamber of sputtering system. Load lock chamber was maintained at a vacuum state for one hour to remove moisture or volatile impurities contained in liquids. When impurity removal is complete, carbon containing solvents were transferred to main chamber and sputtering was proceeded. Pure Pt and Co target was located 20 cm away from the liquid substrate.

Pt sputtering was conducted with a power of 100 W for 20 minutes and simultaneous Co sputtering was conducted with a power of 300 W for 20 minutes, after 30 minutes pre-sputtering of both targets for target cleaning. Particles dispersed in solvents were collected by ethanol filtering. After filtering with ethanol, the samples were dried at 75°C for 5 hours. Then the samples were heat treated under air for 2 hours and continuously in reducing atmosphere for additional 2 hours at 160 °C to remove surface impurities.

Acid treatment in 1 M H_2SO_4 and 1 M HNO_3 solution for 3 hours was conducted to eliminate surface oxides.

PtNi alloy nanoparticles were prepared through identical method, except Co target was replaced by pure Ni (99.95 %) target and sputtering duration was expanded from 20 minutes to one hour.

Schematic image of co-sputtering is illustrated in figure 2.1.

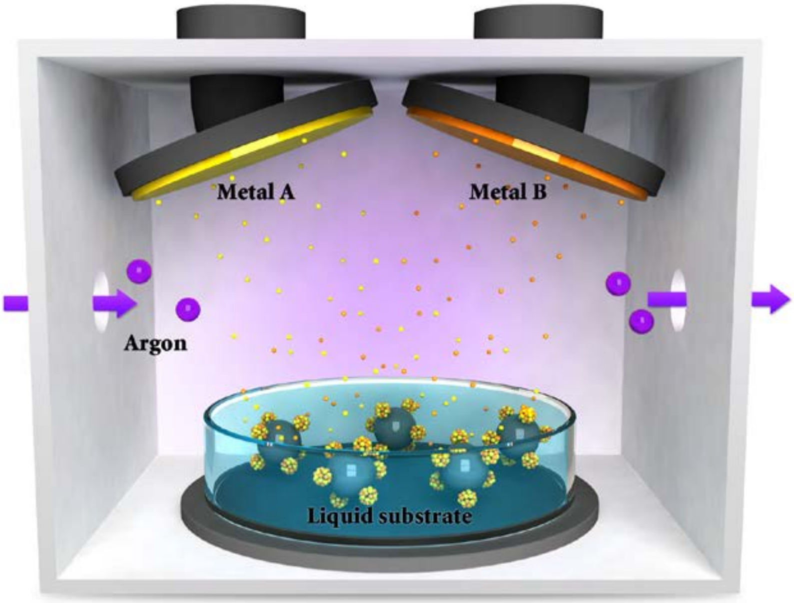

Figure 2. 1 Systematic diagram of co-sputtering on liquid substrate

2.1.4. Carbon supported Pt@Co nanoparticles

Platinum(II) acetylacetonate (Pt(acac)$_2$, 97 %) was purchased from Sigma-Aldrich. Microwave synthesis was conducted by Discover System from CEM Corporation.

Core-shell structure was synthesized through modified liquid sputtering method with assist of microwave instrument. Cobalt seed was prepared by as mentioned liquid sputtering method and platinum shell was deposited onto cobalt seed by microwave deposition.

PEG without carbon supports was set into load lock chamber of sputtering system and maintained in vacuum for one hour. When impurity removal is complete, PEG was transferred to main chamber and sputtering was proceeded. Co sputtering was conducted with a power of 300 W for 20 minutes, after 30 minutes pre-sputtering for target cleaning.

Cobalt nanoparticle containing PEG and Pt precursor containing ethylene glycol (60 mL) was put together into microwave vial and stirred several hours for homogeneous mixing. Amounts of Pt precursor were varied from 2.5 mg to 60 mg in order to control shell thickness.

Homogeneously mixed solvent in microwave vial was placed in microwave and then heated with 140 W until temperature reaches 160°C; approximately 6 minutes are required to get proposed temperature. Carbon supports (20 mg) were injected after temperature drops to 80°C. Carbon supports were dispersed in the solution through one hour sonication, and particles were supported on carbon trough overnight stirring.

Particles dispersed in solvents were collected by ethanol filtering. After filtering with ethanol, the samples were dried at 75°C for 5 hours. Then the samples were heat treated under air for 2 hours and continuously in reducing atmosphere for additional 90 minutes at 160 °C to remove surface impurities.

2.2. Physicochemical characterization

Morphology of prepared samples was observed using high resolution transmission electron microscopy (HR TEM) and scanning transmission electron microscopy (STEM) with energy dispersive spectroscopy (EDS) equipments. For HR TEM analysis, JEM-3000F (JEOL Ltd.) operating at an accelerating voltage of 300 kV was utilized. STEM was acquired by Tecnai F20 (FEI, 200 kV) with EDS made by EDAX and JEM-2100F (JEOL Ltd., 200 kV) with EDS made by Oxford instruments. Total composition of samples and local composition of each particle were also detected by line scan and mapping technique of STEM EDS system.

Zeta potential, the potential difference between the dispersion medium and the stationary layer of fluid attached to the dispersed particle, was obtained using ELS-8000 (Otsuka Electronics Korea). ELS-8000 is electrophoretic light scattering spectrophotometer (ELSS) for measuring Brownian motion of colloidal particles, and zeta potential is calculated from particle movement.

X-ray diffraction (XRD) patterns were obtained using D/MAX 2500 (Rigaku) with Cu Kα radiation (λ=0.1541 nm) at 50 kV and 200 mA. Detection was performed under theta/2theta powder diffraction mode form 20° to 80° (2θ value) at the scan rate of 0.1°/min. XRD spectra allow to detecting not only sample phase but also alloying composition.

Sample composition was further investigated by inductively coupled plasma-atomic emission spectra (ICP-AES) analysis using Shumdzu JP/ICPS-

7500 (Shimadzu), in addition to STEM EDS and XRD. Elemental analysis (EA) of C, H, N through a CHNS-932 (LECO) elemental analyzer, and thermogravimetric analysis (TGA) using TA5000/SDT-Q600 (TA instruments) were also conducted for quantitative analysis of samples. TGA measurements conditions are as follows; temperature was increased from 25 ^{o}C to 800 ^{o}C with a heating rate of 10 ^{o}C/min. 100 sccm of air was flowed during entire detecting period and an alumina sample pan was used.

2.3. Electronic structure characterization

Electronic structures were investigated using X-ray photoelectron spectroscopy (XPS) and X-ray absorption fine structure (XAFS) techniques.

XPS was conducted using Sigma Probe (Thermo) at Al Kα (1486.6 eV) X-ray source. 30 eV pass energy and 0.1 eV step were applied under constant analyzer energy mode. Obtained peaks were deconvoluted with AVANTAGE software, and spectra were calibrated using C 1s peak at 285 eV.

High-resolution XPS (HR-XPS) and XAFS experiments were performed at 8A1 beam line and 7D beam line of Pohang Accelerator Laboratory (PAL), respectively. [1] Synchrotron radiation has various advantages; detecting trace elements, producing 108-fold bright X-rays than from normal X-ray tube and tunable X-ray wavelengths.

8A1 HR-XPS beam line uses soft X-ray beam generated by undulator 6.6 (U6.6) and PHI 3057 electron analyzer. Experiments were conducted at ultrahigh vacuum (UHV) chamber with a base pressure $\leq 5 \times 10^{-10}$ Torr. Therefore, prepared powder samples were adhered on carbon tape, blew several times to remove undetached powder and maintained in vacuum preparing chamber at least 30 minutes. Spectra were measured using 630 eV and 1000 eV of incident photon energy depends on binding energy of materials.

7D XAFS beam line uses 1.4557 Tesla bending magnet as beam source and Si(111) double crystal monochromator. Pt L_3-edge (E_0 = 11564 eV) spectra were obtained in a transmission mode and transmitted beam was detected at He and Ar filled IC Spec ionization chamber. Energy calibration was performed by Pt reference foil. Scan range was divided into 5 sections including both X-ray absorption near edge structure (XANES) and extended X-ray absorption fine structure (EXAFS) region and scan settings were altered according to the section; 5 eV step in region of -200 ~ -50 eV relative to E_0 with 1 seconds of integration time, 1 eV step in region of -50 ~ -20 eV with 1 seconds, 0.3 eV step in region of -20 ~ 40 eV with 1 seconds, 0.03 k step in region of 40 eV ~ 12.0 k with 2 seconds, and 0.05 k step in region of 12.0 k ~ 15.0 k with 2 seconds.

Data analysis was performed with IFEFFIT software; Athena and Artemis. Background (contribution of non-resonant atoms and higher sells) was subtracted using extrapolating pre-edge behavior in the EXAFS region. For EXAFS analysis, normalized oscillatory part of absorption coefficient $\chi(k)$ was determined from measured absorption coefficient, calculated background absorption coefficient and edge step. The normalized oscillatory part was Fourier transformed to R-space with k-weight value of 3. Fourier transformed spectra were fitted using theoretical standards generated with the *ab-initio* FEFF 8.2 code [2].

2.4. Electrochemical characterization

For electrochemical studies, catalyst powder (2.5 mg) was suspended in deionized water (12.5 μL), isopropyl alcohol (375 μL) and 5 % nafion solution (12.5 μL). 15 μL of catalyst ink was pippeted onto the glassy carbon rotating disk electrode (RDE) as a working electrode for the electrochemical experiments. Saturated calomel electrode and Pt wire are served as a reference electrode and a counter electrode, respectively.

Cyclic voltammetry (CV) and linear sweep voltammetry (LSV) were investigated using a PGSTAT30 instrument (Autolab). Electrochemical tests were performed in 0.1 M $HClO_4$ at 293 K with an Ar-purged atmosphere for CV and an O_2-purged atmosphere for LSV with a rotating speed of 1600 rpm, respectively. CO displacement was conducted using cyclic voltammetry method, after high purity CO gas purging for 10 minutes and consecutive Ar gas purging for another 20 minutes. In case of Co_3O_4 catalyst, electrochemical test was performed in 0.1 M KOH solution at 298 K with silver/chloride reference electrode under O_2-saturated atmosphere.

A commercial 40 wt. % and 20 wt. % Pt/C catalyst (Alfa Aesar, a Johnson Matthey company) was used for comparison.

2. 5. References

[1] http://pal.postech.ac.kr/

[2] A. L. Ankudinov, B. Ravel, J. J. Rehr, and S. D. Conradson, "Real-space multiple-scattering calculation and interpretation of x-ray-absorption near-edge structure", *Phys. Rev. B*, **1998**, 58, 7565-7576.

Chapter 3. Results and Discussion

3.1. Establishment of the Liquid Sputtering Method

3.1.1. Sputtering onto ionic liquids

3.1.1.1. Carbon supported metal nanoparticle synthesis

In this chapter, studies on supported metal catalyst synthesis and revealing supporting mechanism were conducted beyond metal nanoparticle synthesis via liquid sputtering method. Inspired by previous research about nanoparticle adsorption on Si [1] or Highly Ordered Pyrolytic Graphite (HOPG) substrate [2] through heat treatment after dropping nanoparticle containing ionic liquid, annealing process was conducted immediately after sputtering under vacuum state, in order to strengthen interaction between supports and nanoparticles.

To reveal the mechanism, equivalent procedures were conducted with various ionic liquids. Commonly used cations, ammonium, pyrrolidinium and imidazolium cation groups, were selected; TMPA and PMPyrd as representative ammonium and pyrrolidinium and 1-alkyl-3-methylimidazolium with 2 to 6 membered alkyl chains as widely used imidazolium were chosen. TFSI was applied for basic anion, but FSI and BF_4 anions were also applied in some cases. Structural formulas and physical properties of low vapor pressure liquids used in experiments are summarized in figure 3.1 and table 3.1, respectively.

Platinum, the most widely used electrocatalyst with outstanding efficiency [3] was selected for sputtering material, in order to directly adopt as practical catalyst.

Synthesis of carbon supported Pt nanoparticle was evaluated through HRTEM images, after Pt sputtering, vacuum annealing and filtering process. In some cases supported metal catalysts were successfully synthesized, while other cases metal nanoparticles were not detached onto carbon supports depending on the types of ionic liquids. Results are shown in from figure 3.2 to figure 3.6. Figure 3.2 represents platinum particles are not supported onto carbon materials using imidazolium group ionic liquids, while figure 3.3 to figure 3.5 shows uniformly dispersed platinum nanoparticles using ammonium and pyrrolidinium group ionic liquids. Observed particles size were 1.89 ± 0.42 nm, 1.82 ± 0.47 nm and 1.72 ± 0.59 nm for TMPA TFSI, PMPyrd TFSI and PMPyrd FSI, respectively.

TEM is a microscopy technique which sharing basic principle with optical microscopy. Electron beam is transmitted through specimen in TEM, instead of visible light in optical microscopy. Observation at a much higher magnification is possible for TEM, since the wavelength of the accelerated electrons is very short compared to the wavelength of visible light, and extremely small amount of specimen is sufficient to be analyzed because the electron beam actively interacts with the substance. In fact, resolution of optical microscopy at 400 nm wavelength light is 150 nm, while resolution of

TEM with 200 kV accelerated electron beam is 0.3 nm. Wavelength of electron beam (de Broglie wavelength of electron) is affected by accelerating voltage as following equations;

$$\lambda = \frac{h}{mv} = \frac{h}{\sqrt{2m_0eE(1+\frac{eE}{2m_0C^2})}}$$

m0 = mass of the electron

e = elementary charge

c = speed of light

E = electric potential

Wavelengths at 100 kV, 200 kV, 500 kV and 1000 kV are 0.0037 nm, 0.00251 nm, 0.00142 and 0.00087 nm, respectively. Therefore, images of few nanometer scale particles were obtained through TEM equipment. [4]

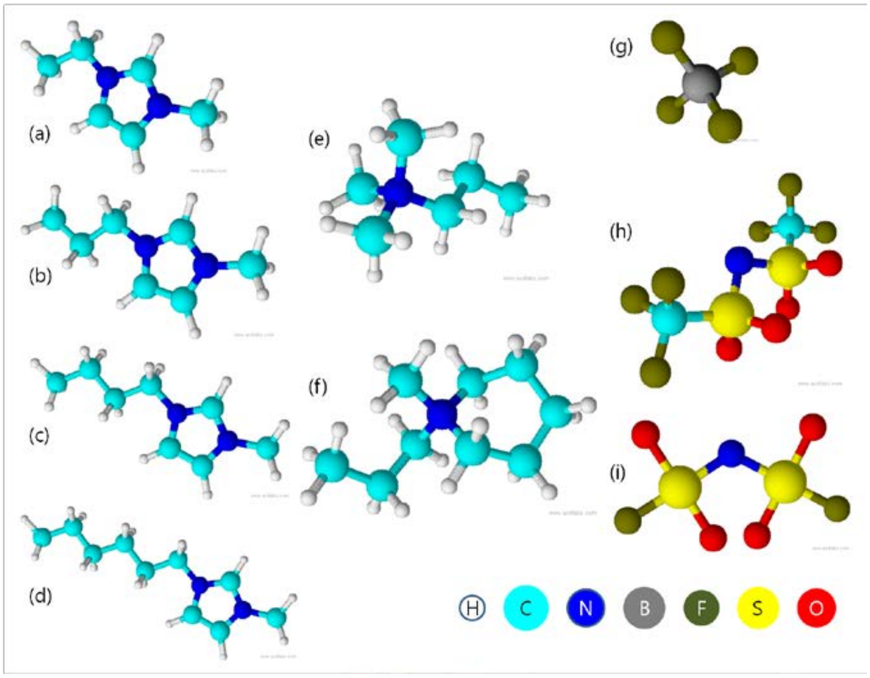

Figure 3. 1 Molecular structures of ionic liquids, (a) EMI, (b) PMI, (c) BMI, (d)HMI, (e) TMPA, (f) PMPyrd, (g) BF_4, (g) TFSI and (i) FSI

I

	Density (g/cm^3)	Viscosity (cp)	Vapor pressure (mmHg)
EMI BF$_4$	1.28 [5]	37 [5]	negligible
EMI TFSI	1.51 [6]	34 [7]	negligible
PMI TFSI	1.475 [8]	-	negligible
BMI TFSI	1.43 [9]	54.5 [10]	negligible
HMI TFSI	1.372 [8]	87.3 [11]	negligible
TMPA TFSI	1.44 [6]	72 [6]	negligible
PMPrd TFSI	1.45 [12]	71.23 [13]	negligible
PMPrd FSI	1.343 [13]	52.7 [13]	negligible

Table 3. 1 Physical properties of ionic liquids and PEG

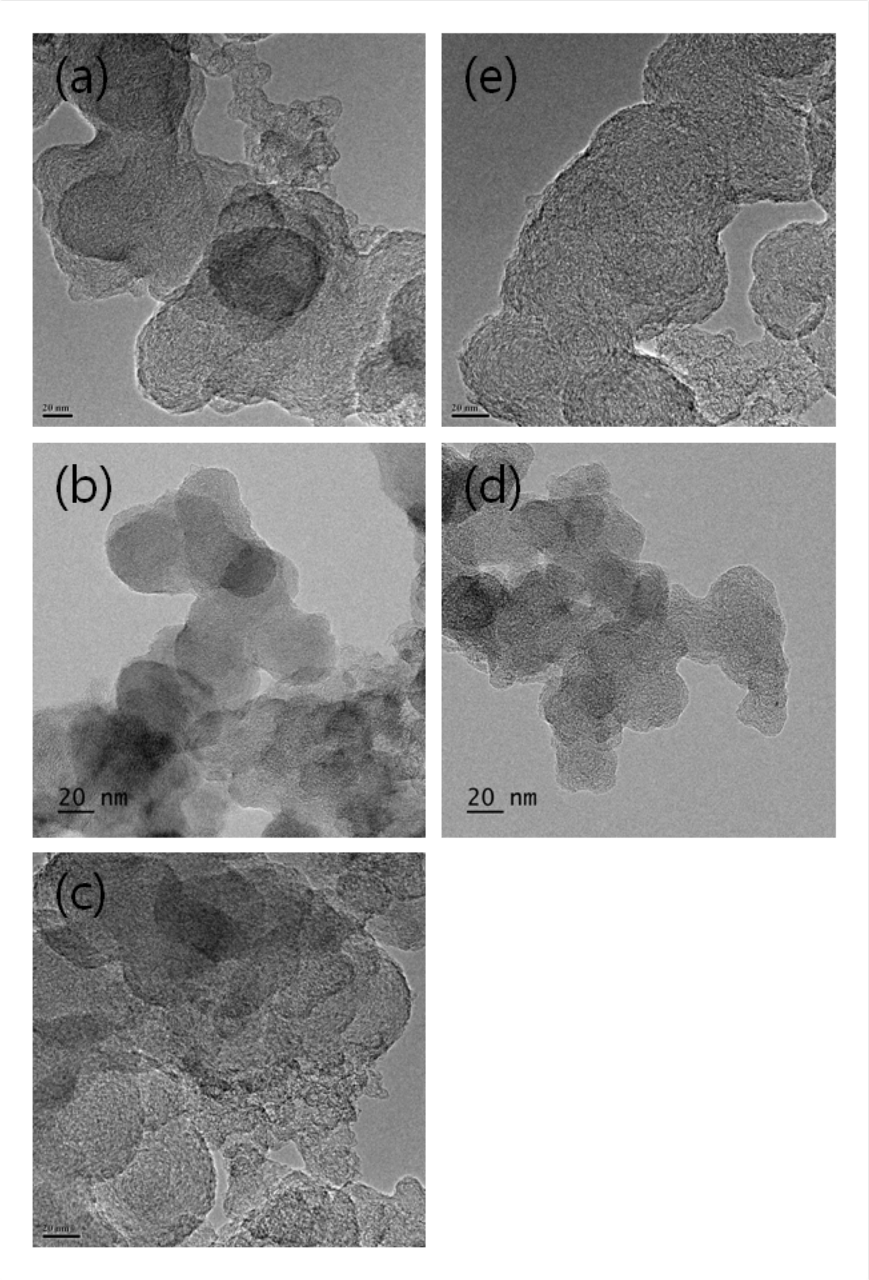

Figure 3. 2HRTEM images of (a) EMI BF$_4$, (b) EMI TFSI, (c) PMI TFSI, (d) BMI TFSI and (e) HMI TFSI

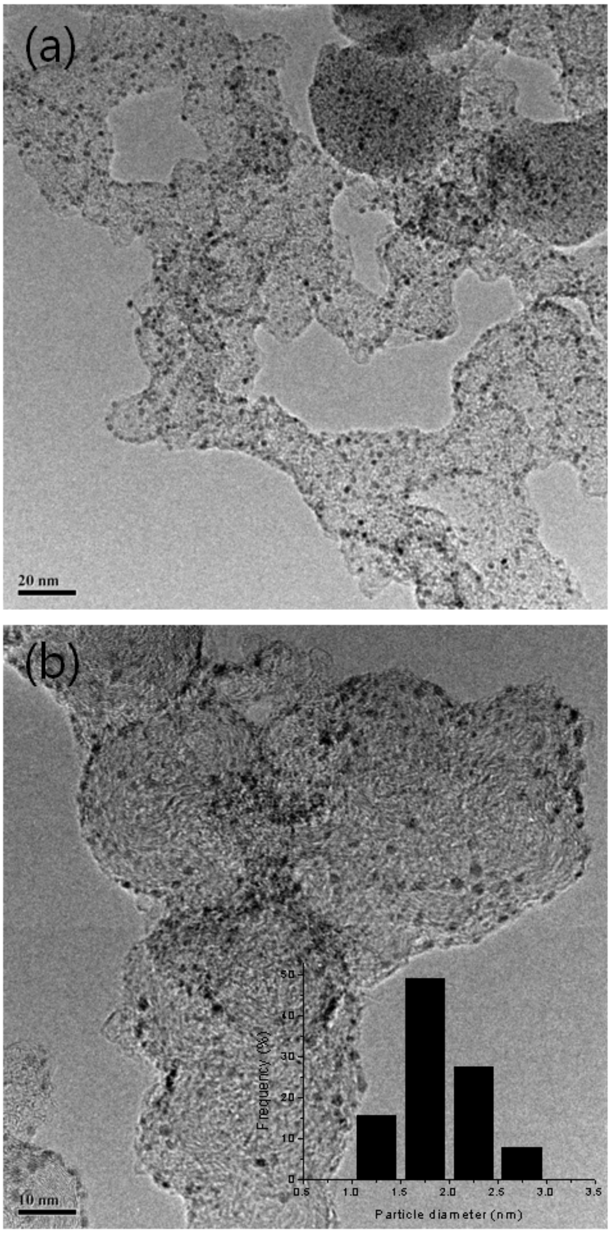

Figure 3. 3 HRTEM images of TMPA TFSI

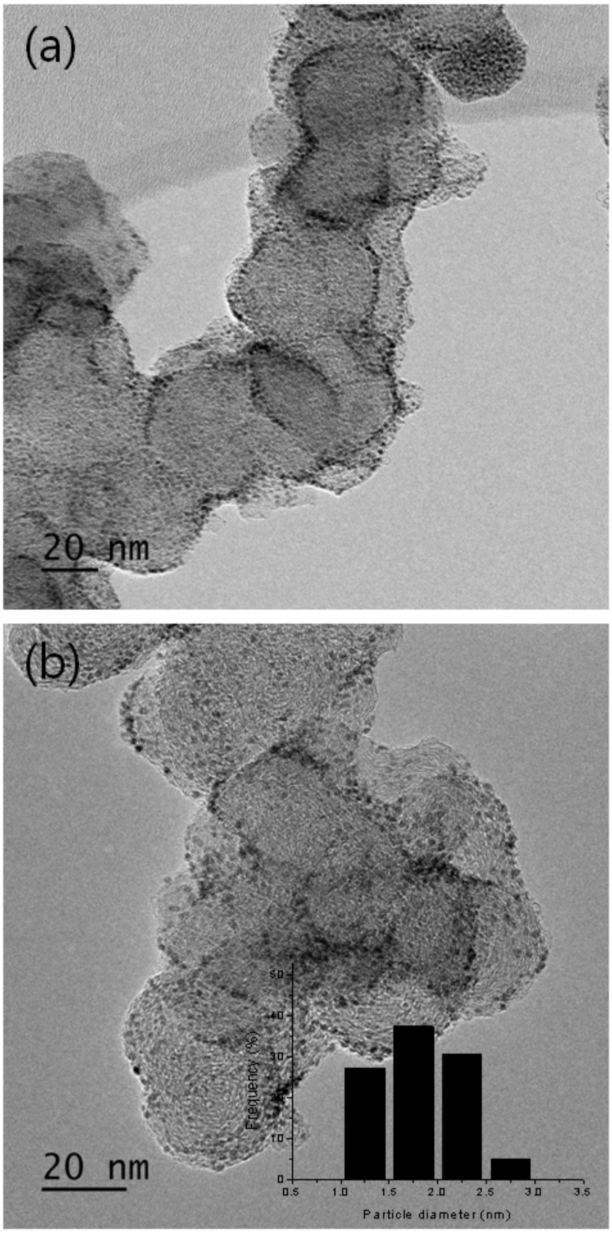

Figure 3. 4 HRTEM images of PMPyrd TFSI

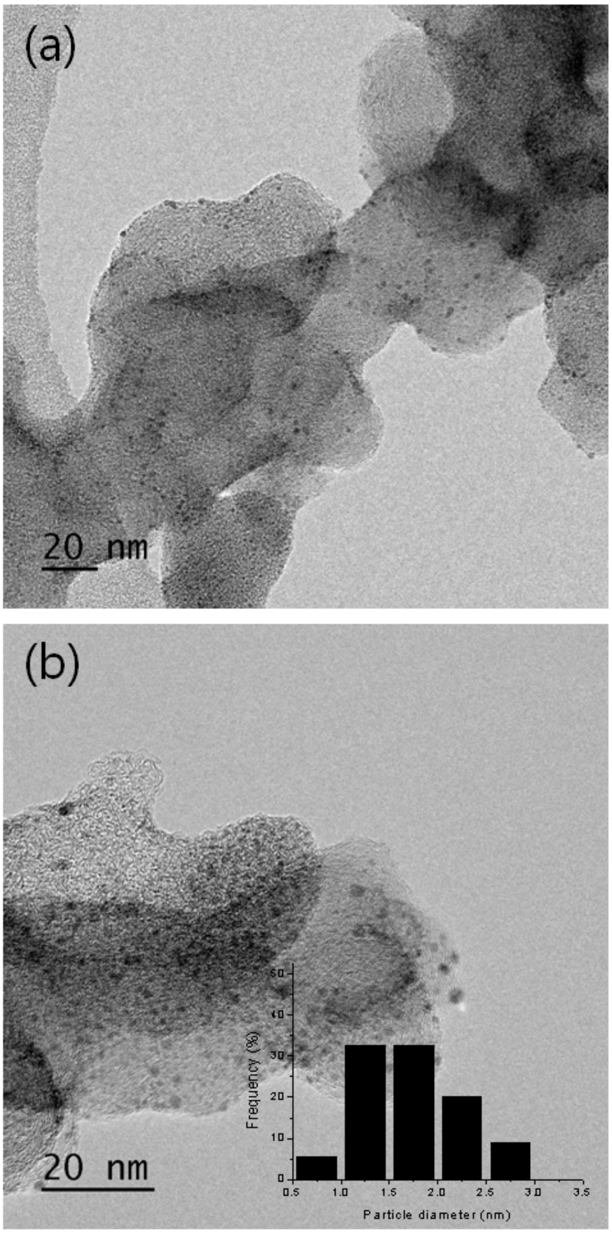

Figure 3. 5 HRTEM images of PMPyrd FSI

3.1.1.2. Supporting mechanism and electrocatalytic activities

In this chapter, metal supporting mechanism was revealed.

It seems that cation plays an important role in supporting mechanism, since metal loading was impossible in imidazolium cation ionic liquid regardless length of alkyl chain or anions according to chapter 3.1.1. However, element analysis of Pt/C prepared using TMPA (one nitrogen atom included) TFSI (one nitrogen atom and two sulfur atoms included) showed opposite results; ratio of N: S was detected to 1.04: 2.00, which means anions are adsorbed on particle surface. Positive zeta potential value (+1.8 mV) calculated from electrophoresis test also reveals that adsorbed ions are anions (figure 3.6). Platinum nanoparticle containing TMPA TFSI solution was obtained by Pt sputtering on TMPA TFSI without support, and 100-fold diluted with ethanol to measure zeta potential.

The following two hypotheses can be established considering supporting is determined by the types of cations, although anions are interacting with and adsorbed on metal particles. ⅰ) Cations are adsorbed on carbon supports and electronic interaction between cations and anions leads metal nanoparticles to be supported. Electronic interaction force is determined by types of ions. ⅱ) Adsorbed anions are directly coupled with carbon supports, however, some kind of cations interfere the coupling by blocking carbon surface (figure 3.7). Steric hindrance effect of bulky pentagonal ring in imidazolium was excluded, because PMPyrd also includes a five membered ring.

According to previous research on cation-anion interaction strength, [14] imidazolium had smaller bonding force than pyrollidinum, in case of same alkyl chain length and anion. However, the difference is not significant and EMI BF_4 has larger bonding force than PMPyrd TFSI. Therefore it is difficult to draw conclusion of ionic bonding force determines nanoparticle supporting. Cation-anion interaction strengths are illustrated in figure 3.8. [14]

Based on previous study, which reveals that aromatic ring of imidazolium strongly adsorbed on carbon surface [15], EA analysis was carried out for carbon supports after dispersed in ionic liquid and vacuum annealed without metal sputtering. Large amount of imidazolium on carbon surface was reaffirmed through the EA analysis; 3 % and 0.3 % nitrogen of carbon was detected for EMI TFSI and PMPyrd TFSI, respectively. Other words, role of cation is not dominant in case of positive charge small nanoparticle supporting in ionic liquids, use of cation which includes aromatic ring and blocks the carbon surface such as imisazolium is not suitable.

It is expected that anions surround metal nanoparticles directly bind with carbon surface. Various functional groups exist on carbon surface, as shown in figure 3.9 (reprinted from [16]). TFSI of FSI includes sulfonyl groups and sulfonyl groups easily react with nucleophiles to remove halide. Unlike FSI, TFSI has $-CF_3$ group next to sulfonyl group, it is also reported that CF_3 groups are easily separated by irradiation. [17] Therefore, it is revealed that supporting mechanism governed by second hypothesis and vacuum annealing process was required to induce chemical reaction between anion and functional group on carbon surface.

XPS analysis of TMPA TFSI Pt/C was carried out to confirm the bonds between anion and functional group. Figure 3.10 (a) and (b) shows C 1s peak of TMPA TFSI Pt/C and PEG Pt/C. TMPA TFSI Pt/C has additional carbon peak at 289 eV. Another two peaks at 285 eV and 286 eV refers to normal hydrocarbons and oxidized carbons on surface respectively. [18] C 1s peak at high binding energy originated from CF_3 in TFSI, when considered with F 1s peak at 689 eV, which refers to C-F bonding. [18] Direct evidence of bonding formation between functional group and anion can be found in S 2p spectra. Since two sulfurs in TFSI present in the symmetric position, only 1 S 2p peak should be appeared, but two separated peaks were measured in figure 3.10 (d). Higher binding energy peak at 168.72 eV originated from sulfonly group [18], while additional peak at 163.87 eV is hard to denominate as sulfonyl group. This range of binding energy refers to SO compounds [18], so it is predicted that sulfonyl group reacted with functional group on carbon surface and build new –S-O-carbon compound bonding; ratio of reacted and unreacted sulfonyl group is 0.95: 1.

Catalytic propertiy of Pt/C catalysts prepared in TMPA TFSI was investigated by various aspects and possibility as practical catalyst was evaluated.

X-ray diffraction is a phenomenon that atomic planes of a crystal cause an incident beam of X-rays to interfere with one another as they leave the crystal. Using this phenomenon crystalline phases and orientation of single crystal or grain can be identified without specimen destruction. This nondestructive technique also finds the crystal structure of unknown materials. Moreover, structure properties, such as lattice parameter, strain, grain size, expitaxy, phase composition and preferred orientation can be determined by XRD.

A diffraction phenomenon occurs, following relationship (Bragg's low) is established between wavelength of incident X-ray beam, incident angle of X-ray and d spacing;

$n \lambda = 2 d \sin \theta$

n = order of the diffraction

λ = wavelength of the X-ray beam

d = interatomic spacing of crystal plane

θ = incident angle of X-ray source

When the relation is applied, interatomic distance at particular plane is calculated, as well as the lattice parameter calculation is possible.

$a = d_{hkl}\sqrt{h^2 + k^2 + l^2}$

a = lattice parameter

d_{hkl} = interatomic spacing at (h k l) plane

The average crystalline size (L) of the nanoparticles was determined using the Scherrer equation.

$$L = \frac{0.9\lambda_{K\alpha}}{B(2\theta)\cos\theta_{max}}$$

$\lambda_{K\alpha}$ = Cu Kα beamline as the X-ray source from a X-ray generator

$B(2\theta)$ = full width at half maximum (FWHM) in radians

θ_{max} = angle value of the specific crystal plane at maximum intensity.

In figure 3.11, the XRD patterns of both synthesized Pt/C and commercial Pt/C showed three main peaks of face centered cubic (FCC) Pt crystalline phase, (111), (200), and (220) at 39.8°, 46.2°, and 67.5°, respectively (JCPDS file no. 87-0640). The average size of platinum nanoparticles was calculated from XRD patterns with the Scherrer equation. It was 1.94 nm and 3.72 nm for TMPA TFSI Pt/C Pt/CNT and commercial Pt/C, respectively. Although calculated values are not exactly match with estimated value from TEM images, equal tendency was confirmed. Lattice parameters and interatomic distances were maintained at the same value, since prepared sample contained single platinum element and XRD peak shift was not observed.

TGA applies temperature program to the sample and measures changes in mass of the sample as a function of time and temperature. Mass loss is generated by evaporation or gas phase product generation by chemical reactions. Decomposition behaviors are revealed by reaction of samples with gas (oxygen, air), such as oxidative decomposition reaction with purged oxygen. The mass changes are continuously measured by the sensitive electronic balance. Using TGA, metal loading amount versus carbon supports are detected under continuous air gas purging. Platinum metal loading amount of sample was approximately 25 %; exact measuring of platinum loading amount was difficult, due to as mentioned surface adsorption of ions. Figure 3.12, TMPA TFSI Pt/C sample experienced large mass change twice. The second mass change was oxidation of carbon supports, but first mass change originated in oxidation of residue ions. Ignoring first mass variation under 400 ℃, platinum loading amount was estimated about 25 %. This TGA result is coincident with as mentioned anion adsorption.

Successful platinum nanoparticle synthesis was confirmed by TEM and XRD, electrochemical performance was evaluated for catalyst application. Electrochemical characterization was carried out in 0.1 M $HClO_4$ at 20 ℃.

In case of TMPA TFSI Pt/C, characteristic peaks of Pt/C were disappeared due to as mentioned strong anion adsorption on metal surface; Platinum surface is not actually contact with electrolyte. As a result, surface reaction cannot occur. Polarization curve obtained via RDE in O_2 saturated 0.1 M $HClO_4$ electrolyte also revealed strong ion adsorption on TMPA TFSI Pt/C surface.

It was concluded that Pt/C nanoparticles were successfully synthesized via direct sputtering onto ionic liquid substrates and revealed their supporting mechanism. However, prepared nanoparticles were not suitable for electrochemical catalysts due to strong adsorption of ions; adsorbed ions are expected to act as surfactant, despite of no additional surfactant was added.

Therefore proper synthesis for electrochemical catalyst will be investigated in next chapter.

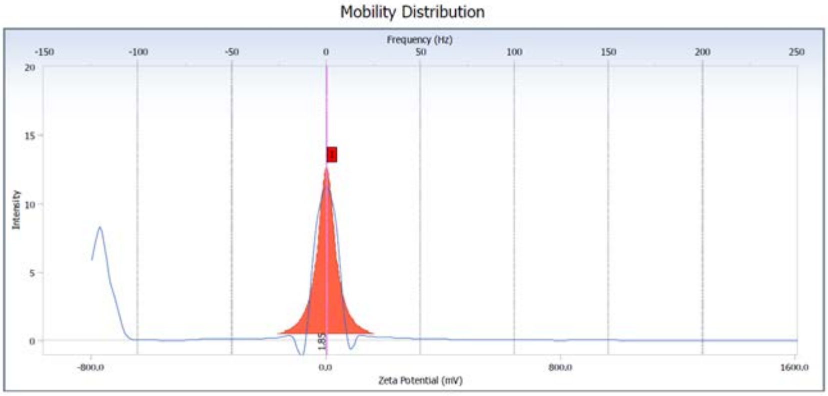

Figure 3. 6 Measured zeta potential

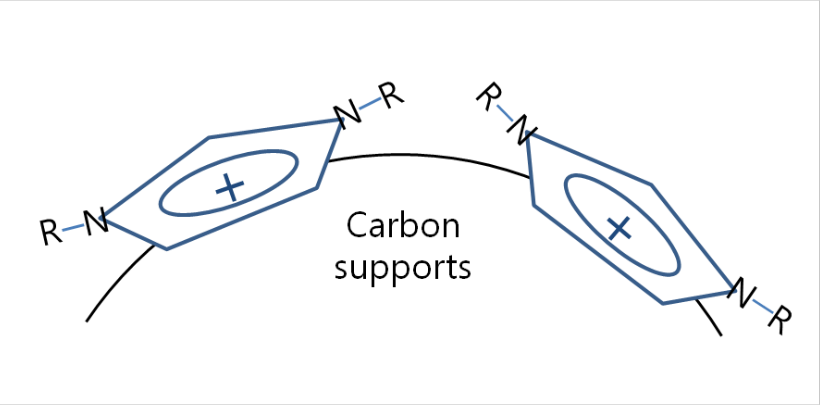

Figure 3. 7 Diagram of carbon surface adsorbed imidazolium cation

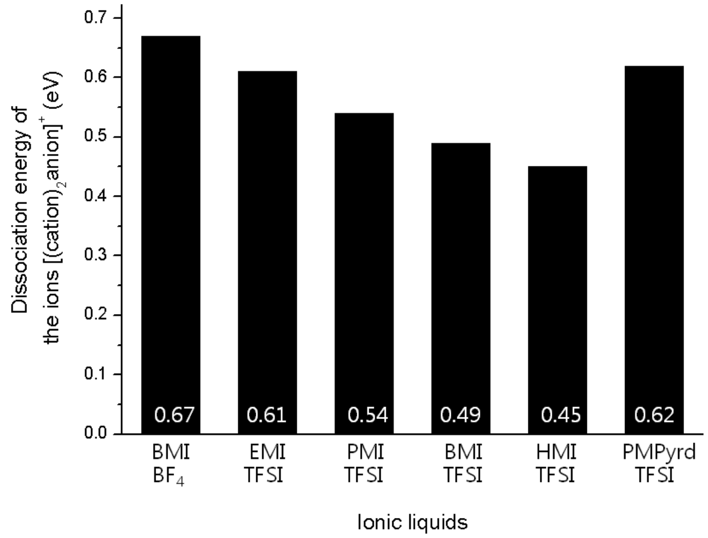

Figure 3. 8 Dissociation energies of various ionic liquids

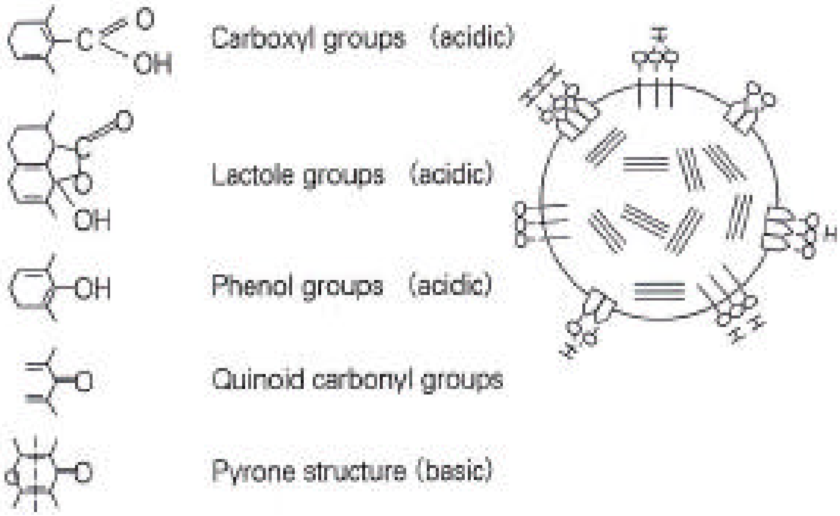

Figure 3. 9 Functional groups on carbon black surface

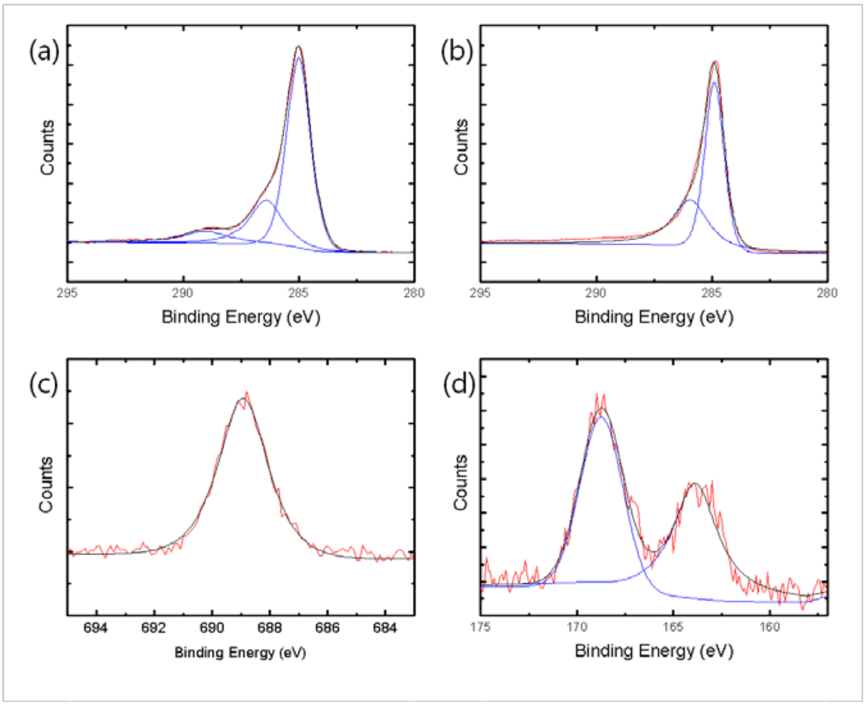

Figure 3. 10 XPS spectra from (a) C 1s of IL Pt/C, (b) C 2s PEG Pt/C, (c) F 1s and (d) S 2p of IL Pt/C

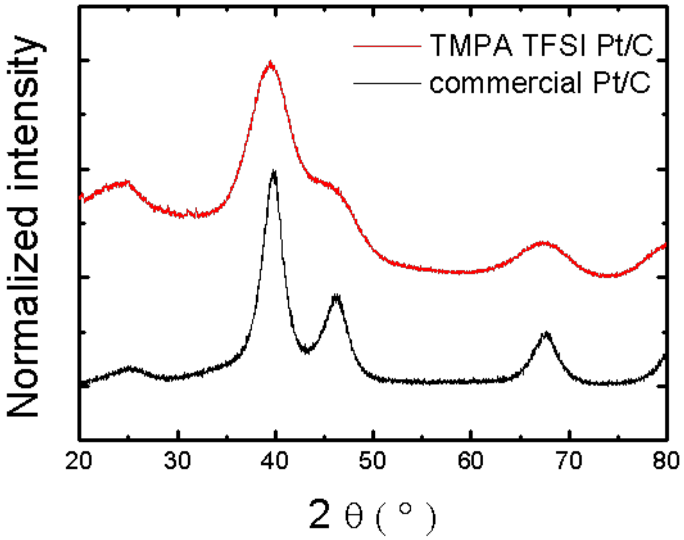

Figure 3. 11 XRD diffraction patterns from TMPA TFSI Pt/C and commercial Pt/C

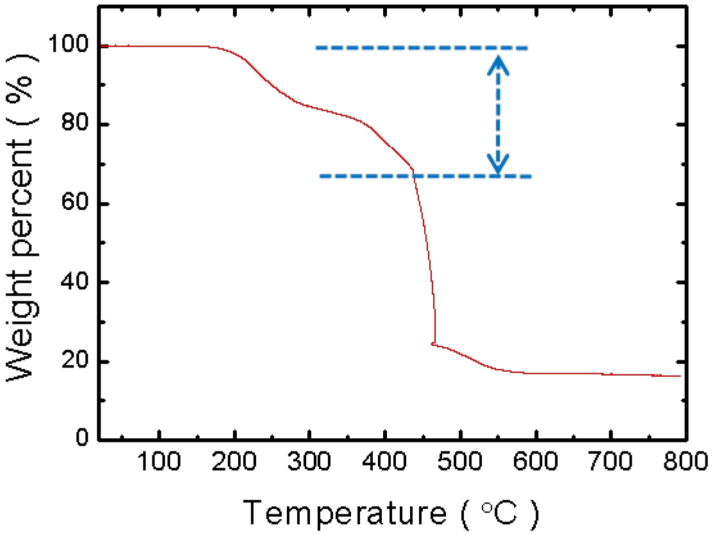

Figure 3. 12 TG analysis result from TMPA TFSI Pt/C

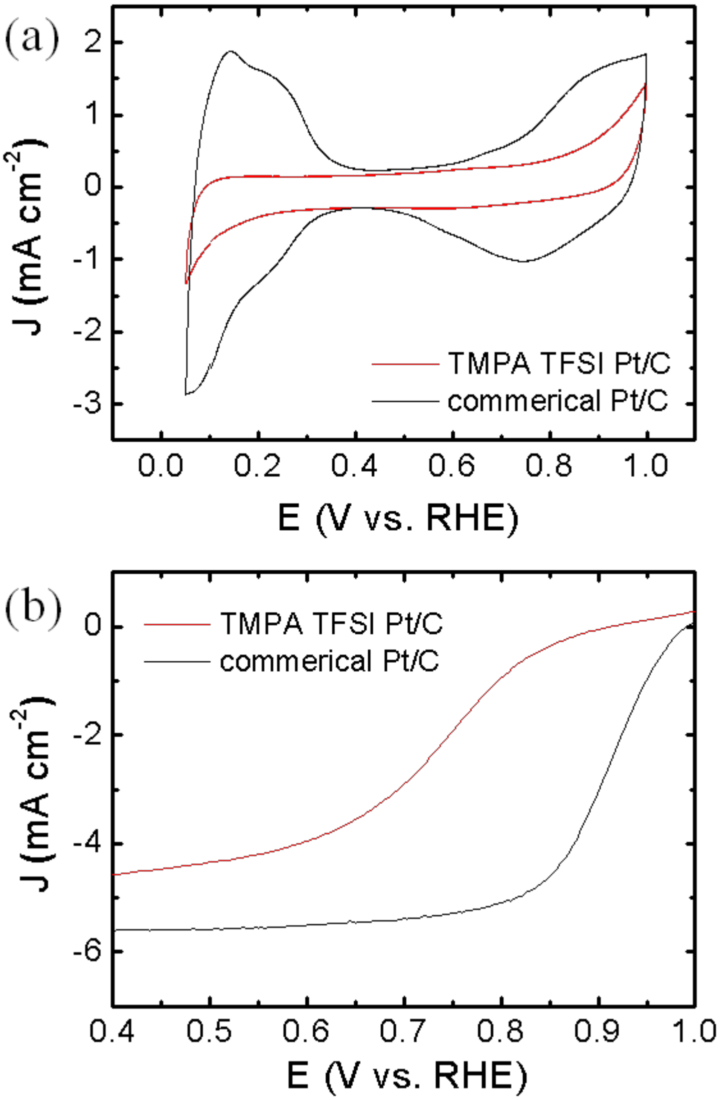

Figure 3. 13 (a) Cyclic voltammograms and (b) ORR polarization curves from Pt/Cs

3.1.2. Sputtering onto PEG

Environmental friendly and cost effective PEG was chosen for alternative of ionic liquids. Physical properties of PEG600 are as follows; 1.12 g/cm^3 of density, 135 cp of viscosity and <0.01 mmHg vapor pressure at room temperature. [19]

Unlike the cases of ionic liquids, supported platinum nanoparticle were easily synthesized by just sputtering onto carbon containing PEG solvents due to the Van der Waals force. Obtained particles had average sized of 2.00 ± 0.51nm. It indicates that the liquid sputtering synthesis leads well dispersed uniform nanoparticle formation, without surfactant.

Figure 3.14 TEM image shows spherically shaped metal NPs on carbon supports with an average diameter of 2.0 ± 0.5 nm, whereas commercial Pt/C was an average size of 2.7 ± 0.8 nm, which showed slightly larger size and broader distribution than the synthesized NPs. This indicates that no agglomeration occurred during filtration and heat treatment without additional surfactant, and that simple sputtering synthesis allows for preparing NPs with superior distribution compared to commercial NPs. Additional Pt/CNT (carbon nanotube) was synthesized with PEG solvent and average particle size was 1.6 ± 0.6 nm (figure 3.15). Acid treatment of CNT was carried out for better dispersion.

In figure 3.16, the XRD patterns of both synthesized Pt/C and commercial Pt/C showed three main peaks of face centered cubic (FCC) Pt crystalline phase, (111), (200), and (220) at 39.8°, 46.2°, and 67.5°, respectively (JCPDS file no. 87-0640). The average size of platinum nanoparticles was calculated from XRD patterns with the Scherrer equation. It was 2.2 nm, 1.1. nm and 3.72 nm for PEG Pt/C, PEG Pt/CNT and commercial Pt/C, respectively. Although calculated values are not exactly match with estimated value from TEM images, equal tendency was confirmed. Lattice parameters and interatomic distances were maintained at the same value, since all prepared samples contained single platinum element and XRD peak shift was not observed.

Using TGA, metal loading amount versus carbon supports are detected under continuous air gas purging. Platinum metal loading amount of samples were 27 % and 36 % for PEG Pt/C and PEG Pt/CNT, respectively. Figure 3.17, PEG samples underwent one significant mass change over 400 ℃ which was caused by oxidation of carbon supports, unlike ionic liquids in previous chapter.

Successful platinum nanoparticle synthesis was confirmed by TEM and XRD, electrochemical performance was evaluated for catalyst application. Electrochemical characterization was carried out in 0.1 M $HClO_4$ at 20 ℃.

Typical cyclic voltammetgrams of Pt/C catalyst were obtained for PEG samples, since all prepared catalysts were platinum single component materials; H_{upd} peak under 0.4 V and platinum oxidation peak near 0.8 V was observed. Clear CO oxidation peaks were also detected. CO oxidation peak of PEG Pt/CNT shifted negatively, this is common phenomenon for CNT supports due to the following reason. [20] CNT has high graphitic crystallinity and high density of surface functional groups and this leads to anchor nanoparticles and strengthen the metal nanoparticle-support interaction. Strong metal-support interaction is beneficial for electron transfer during the electro-chemical reaction. Fast electron transfer causes earlier oxidation of surface adsorbed CO molecules. In addition to negative shift of CO oxidation peak, reduced particle size and higher loading amount by anchoring effect were also observed in CNT sample.

Polarization curves were obtained via RDE in O_2 saturated 0.1 M $HClO_4$ electrolyte. Because single platinum material was used, the prepared samples exhibited similar performance. Comparing with 40 wt. % commercial Pt/C catalyst, slightly inferior catalytic activity was detected and the two main reasons for lower activity can be given; lower metal loading and smaller particle size. It has been reported that 3 nm diameter platinum nanoparticles, which have a sufficient terrace site proportion, displayed maximum catalytic activity [21], and commercial Pt/C has more of this diameter range than that of synthesized platinum nanoparticles. Despite the advantage of rapid CO oxidation reaction and higher loading amount than PEG Pt/C, PEG Pt/CNT cannot exhibit outstanding performance due to the smallest particle size among samples. Potential of zero total charge test reaffirmed higher PZTC voltage of commercial Pt/C than PEG Pt/C, which means superior catalytic activity of commercial Pt/C.

Even though slightly inferior activity than commercial catalyst, the synthesized supported nanoparticles showed catalytic applicability and performance could be enhanced by adjusting particle sized or composition.

Comparing ionic liquids and PEG, there is no significant difference in particle size or distribution, even though PEG is less expensive and more eco-friendly than ionic liquids and PEG does not require extra annealing step for supporting. Moreover, nanoparticles prepared with PEG overcome the limitation of ionic liquids. We believed that PEG sputtering method could be a promising method for preparing carbon supported nanoparticles.

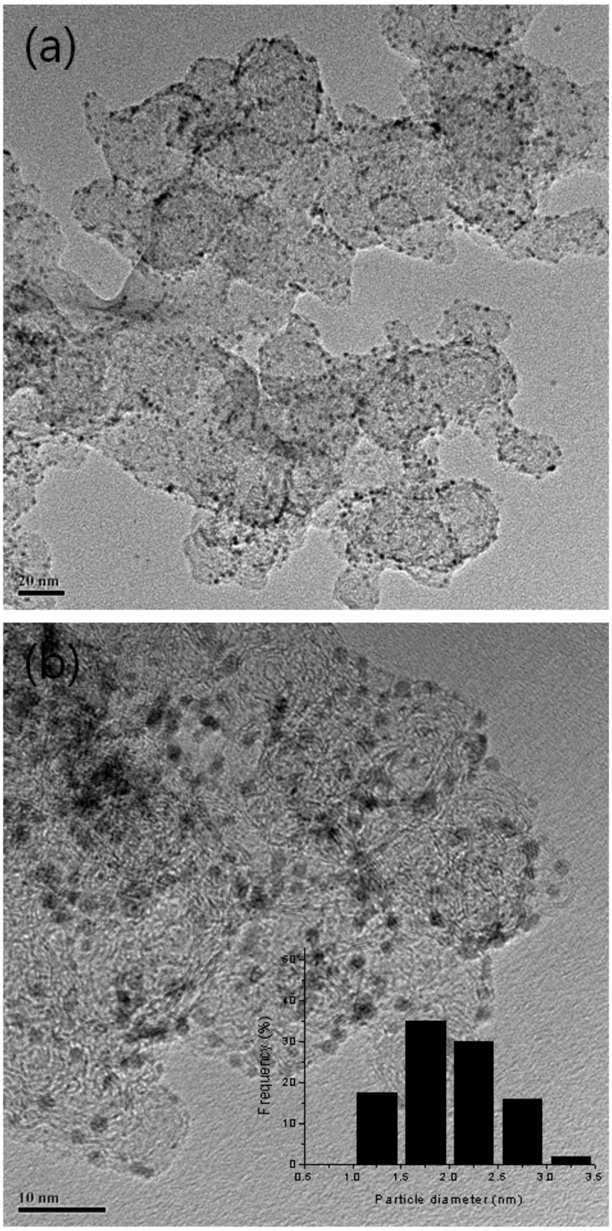

Figure 3. 14 HRTEM images of Pt/C

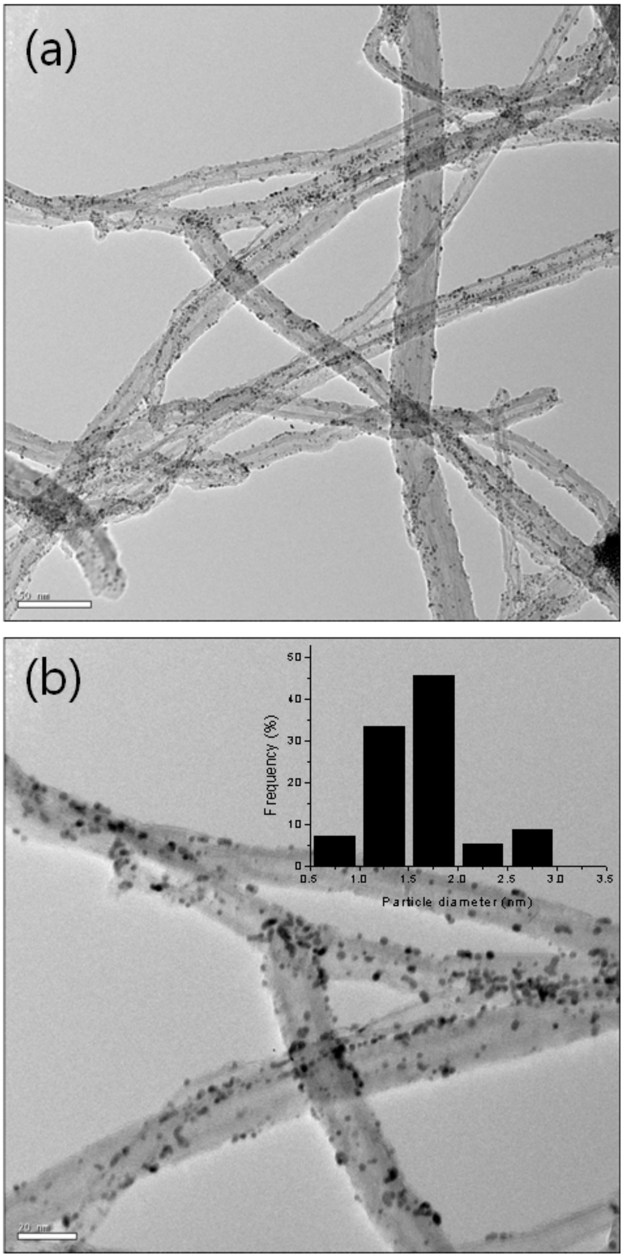

Figure 3. 15 HRTEM images of Pt/CNT

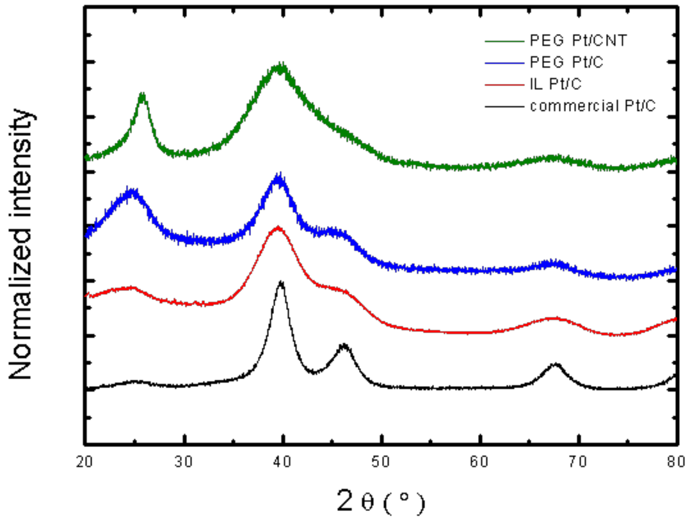

Figure 3. 16 XRD diffration patterns from various Pt/C samples

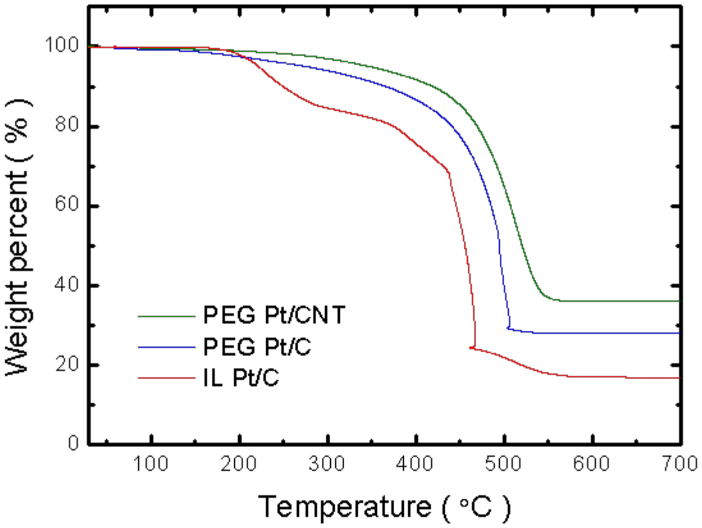

Figure 3. 17 TG analysis results from Pt/Cs

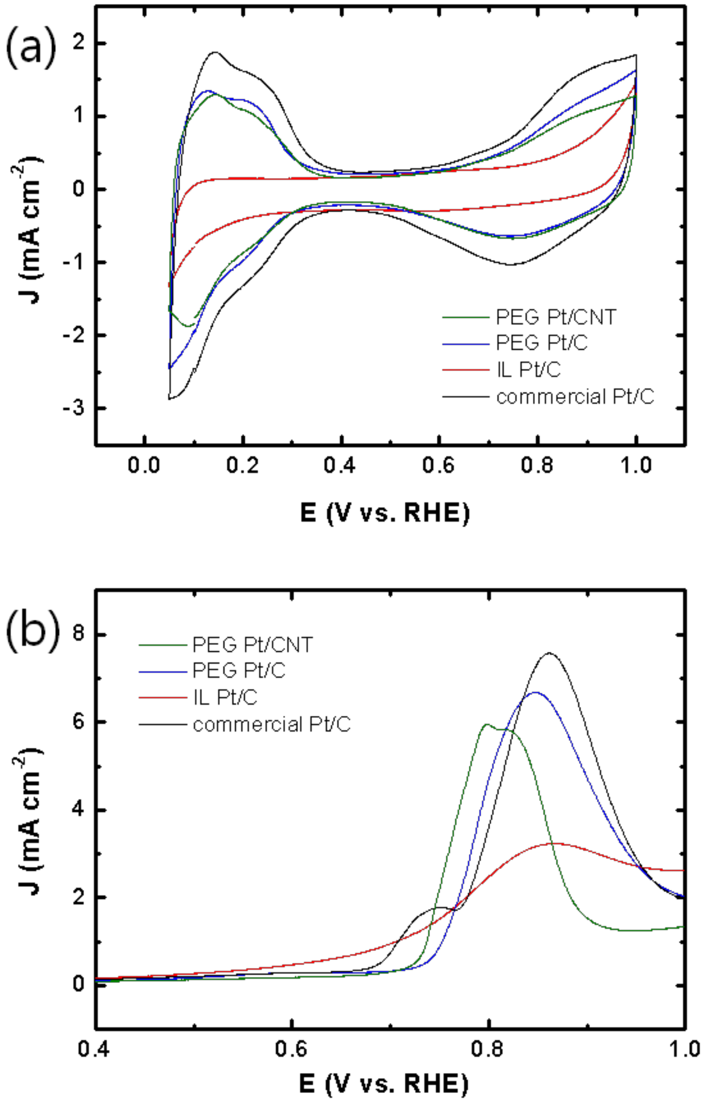

Figure 3. 18 (a) Cyclic voltammograms and (b) CO stripping curves from Pt/Cs

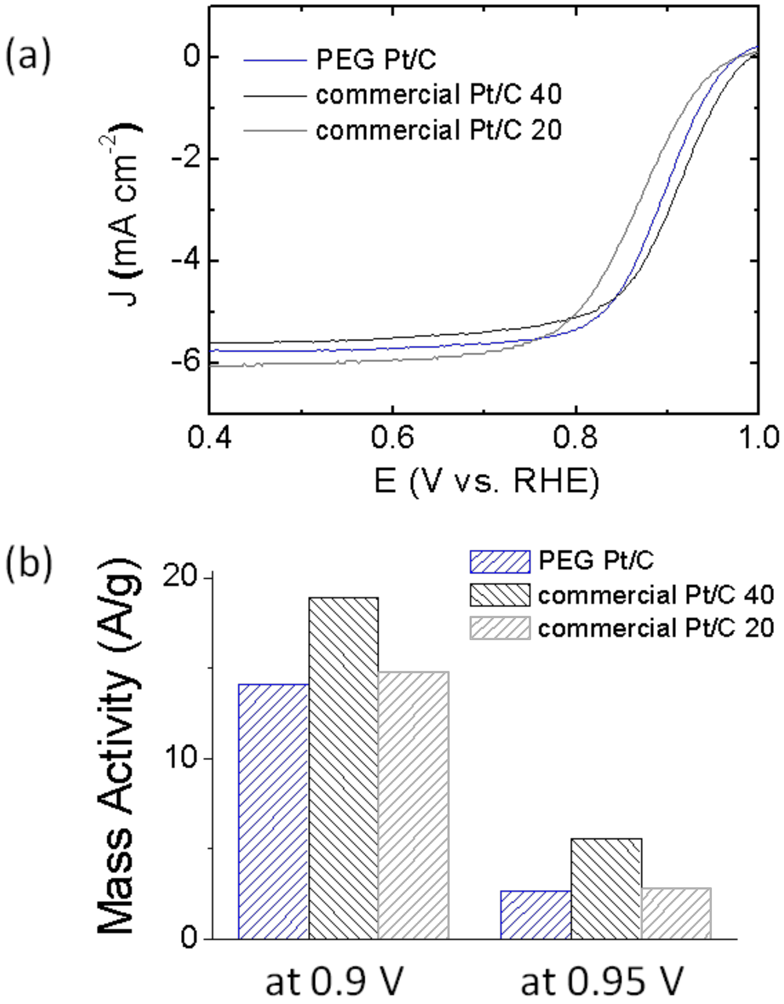

Figure 3. 19 (a) ORR polarization curves from Pt/Cs and (b) their mass activities

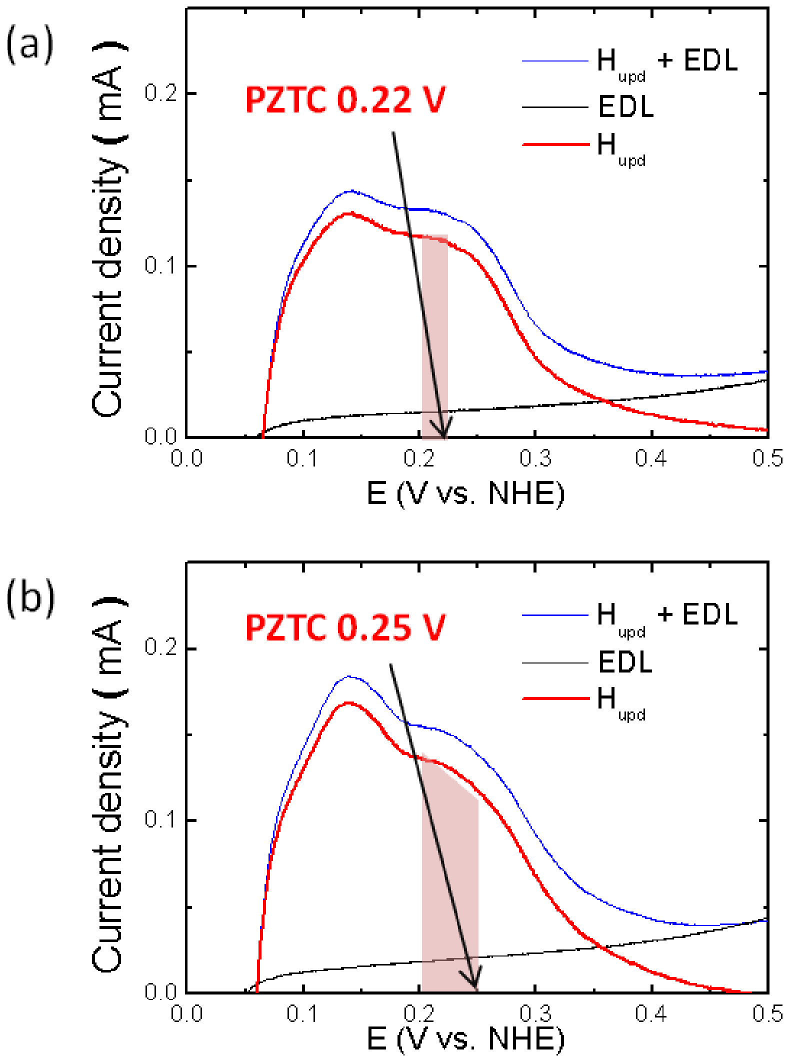

Figure 3. 20 (a) PZTC of PEG Pt/C and (b) commercial Pt/C

3.2. Applications of the Liquid Sputtering Method

3.2.1. Alloy nanoparticles via co-sputtering

In order to reduce the use of platinum and enhance the catalytic activity, Pt-based multi-metallic catalysts had been intensively studied. In this chapter, binary alloy metal nanoparticles were synthesized via simple co-sputtering method and structural and electrochemical properties were investigated. Cobalt and nickel, known to show high performance, were selected for alloying material. Experimental procedure is identical with 3.1.1, except simultaneous sputtering of two separated targets and additional acid treatment.

Morphology, size and composition of the prepared samples were investigated by HRTEM, STEM EDS and ICP analysis. PtCo/C and PtNi/C fabricated through sputtering techniques onto the PEG substrate were shown in figure 3.21 and figure 3.22. Spherical shaped metal NPs were well distributed on carbon supports with a narrow size distribution. Average diameters were 2.0 ± 0.4 nm and 2.0 ± 0.4 nm for PtCo/C and PtNi/C, respectively. EDS mapping and line scan results confirmed that Pt and Co or Ni atoms co-exist in one alloy nanoparticle rather than Pt and Co or Ni atoms are separated on carbon supports as observed in figure 3.23. The ratios of Pt to 3-d transition metal element in prepared platinum alloy nanoparticles were calculated to be 3.4: 1 for PtCo/C and 3.6: 1 for PtNi/C by ICP analysis and Pt_3M_1/C is well-known to display the best oxygen reduction activity. [22]

Phase structures of platinum alloy nanoparticles were studied using X-ray diffraction patterns in figure 3.24. Observed three main diffraction peaks refer to (1 1 1), (2 0 0) and (2 2 0) planes of face centered cubic structures and the XRD patterns of both platinum alloyed nanocatalysts showed high angle shifted peaks compared to the platinum single component sample. Replacement of platinum atom by smaller cobalt or nickel atoms leads to lattice parameter reduction which causes high angle shift of diffraction peaks. In other words, peak shift in XRD patterns means successful alloy formation. [23]

Ratio of Pt: Co in the synthesized PtCo/C was directly estimated to 3: 1 since diffraction peaks of the PtCo/C coincide with already indexed Pt_3Co composition. The value is also agreed with ICP analysis. Although diffraction peaks of PtNi/C do not match with indexed patterns, composition can be estimated using degree of peak shift. Lattice parameters from shifted peak positions are as follows; 3.92 Å for Pt (JCPDS file no. 87-0640), 3.54 Å for Co (JCPDS file no. 01-089-7093), 3.52 Å for Ni (JCPDS file no. 87-0712), 3.85 Å for Pt3Co (JCPDS file no. 29-0499), 3.85 Å for synthesized PtCo/C and 3.83 Å for synthesized PtNi/C (calculated from XRD patterns). Cooperation degree of nickel was calculated using Vegard’s law.

$$a_{A_xB_{1-x}} = xa_A + (1-x)a_B$$

$$x = \frac{(a_{A_xB_{1-x}} - a_B)}{(a_A - a_b)}$$

Obtained composition was $Pt_{3.35}Ni_1$ and it was also well agreed with ICP analysis. The XRD and STEM EDS data indicated that simple co-sputtering could be an easy synthesis method for alloy nanoparticles. Average particle size was estimated by Scherrer equation with (220) peak in XRD patterns. It was 2.8 nm and 1.8 nm for PtCo/C and PtNi/C, respectivley.

Electrochemical results were acquired to evaluate ORR activity of prepared samples, and summarized in figure 3.25 and figure 3.26. Altered electronic properties due to the presence of the non-noble metal cause adsorption behavior variations. Adsorption strengths of platinum alloyed with 3-d transition metal normally weaken compared to monometallic platinum and weakened interaction is believed to the origin of the enhanced ORR activity. Hydrogen underpotential deposition (H_{upd}) peak shape change or negative shift and broadening of CO oxidation peak are occurred when electronic properties were altered. [24] H_{upd} and CO oxidation peak change was observed in both PtCo/C and PtNi/C samples. Altered binding energy between adsorbed species and platinum due to changes in electronic structure was confirmed via CV and CV stripping analysis, consequently improved ORR activity can be predicted. Half wave potential of PtNi/C was shifted 17 mV toward positive direction and mass activity at 0.95 V was 3.6-fold increased compared with Pt/C catalyst. Detailed values of ESCA, half wave potential and mass activity at 0.9 V and 0.95 V are listed in table 3.2.

For further insight into the electronic structures of alloyed catalysts, XAFS measurements were carried out. Calculated atomic distances and coordination numbers from fitted extended X-ray absorption fine structure (EXAFS) data are listed in Table 3.3. FEFF program was used for data reduction and analysis.[25] Data and fits of the magnitude of Fourier transformed k3-weighted EXAFS spectra are shown in figure 3.27 (a). The decreased Pt-Pt lattice from the Co or Ni alloying effect induced overlapping of the Pt d-bands, thus the activity for ORR could be enhanced due to weakening binding forces between metal NP and oxygen species. [26] According to the X-ray absorption near edge spectroscopy (XANES) data in figure 3.27 (b), increased white line intensities in the PtCo or PtNi alloy sample were observed. However, a reduction in the Pt white line is usually found in platinum alloy materials due to electron transfer from 3-d transition metal to Pt, and it becomes one of the reasons for the increased ORR performance. [27] This opposite trend in the prepared samples is originated from inserted sub-monolayer oxygen [28] as identified by EXAFS result, which causes interruption of white line intensity.

Electron transfer can be also explained by the binding energy of XPS analysis, according to the report published by Watanabe’s group. [29] In general, a positive shift of core level XPS has been interpreted to electron loss of atoms. However, this conventional explanation does not match with theoretically estimated electron transfer direction, electron transfer should occur from cobalt or nickel to platinum atom. An alternative explanation was suggested based on rehybridization of the d-band as well as the sp-band. The work function change due to electron transfer to platinum atom leads to the reference level upshift in photoelectron measurement. This upshift causes downshift of Pt 4f core level and d-band center (figure 3.28, reprinted from [29]). Positive shift of Pt 4f peak was observed in figure 3.29 for both alloy samples; 0.3 V for PtCo/C and 0.5 V for PtNi/C. Thus, this increase in binding energy could be more clear evidence of electron transfer from cobalt or nickel to platinum atom.

Alloy nanoparticles were synthesized via simple co-sputtering onto PEG substrate, and alloy formation was clearly confirmed by various techniques such as STEM EDS, XRD, XAFS and XPS. Electron transfer and lattice decrease were also demonstrated and enhanced ORR performance was measured.

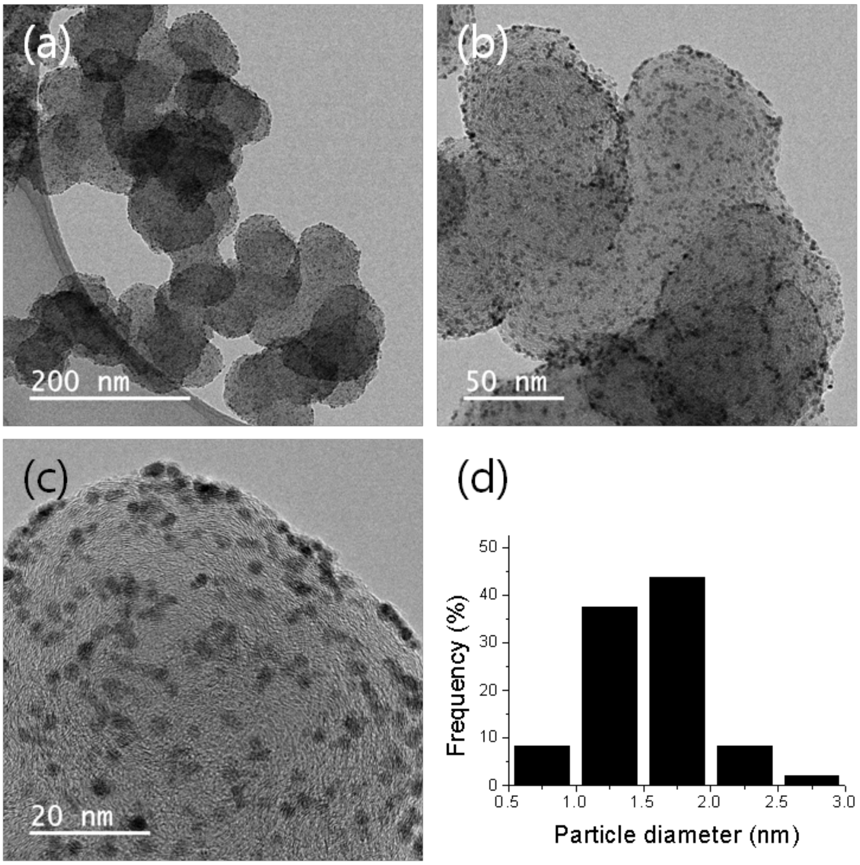

Figure 3. 21 HRTEM images of PtCo/C and their size distribution

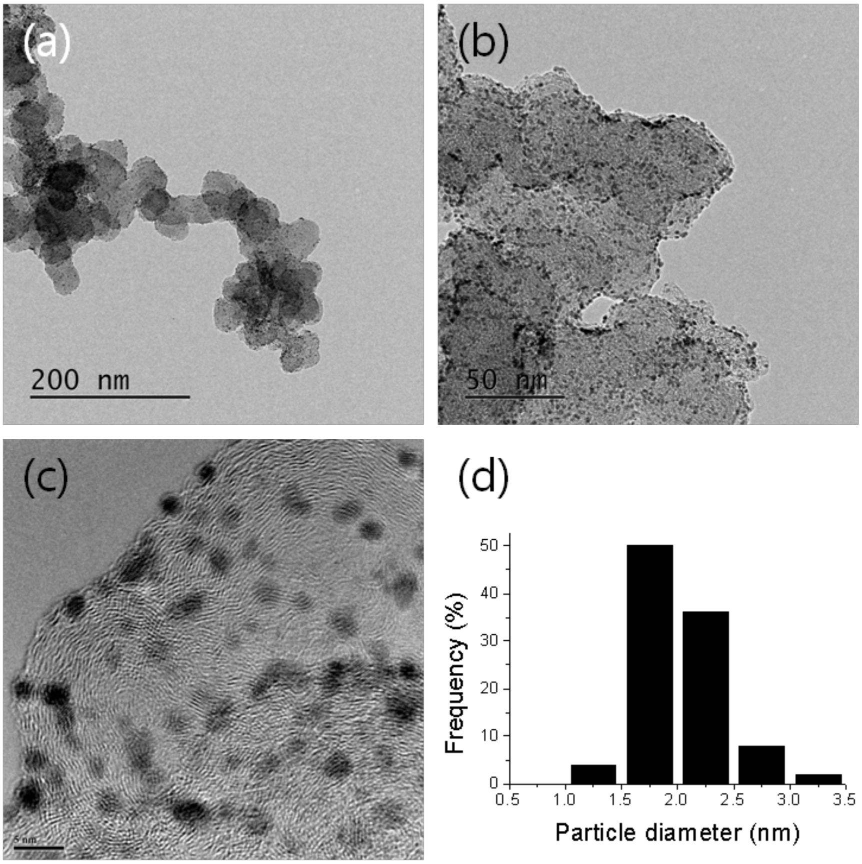

Figure 3. 22 HRTEM images of PtNi/C and their size distribution

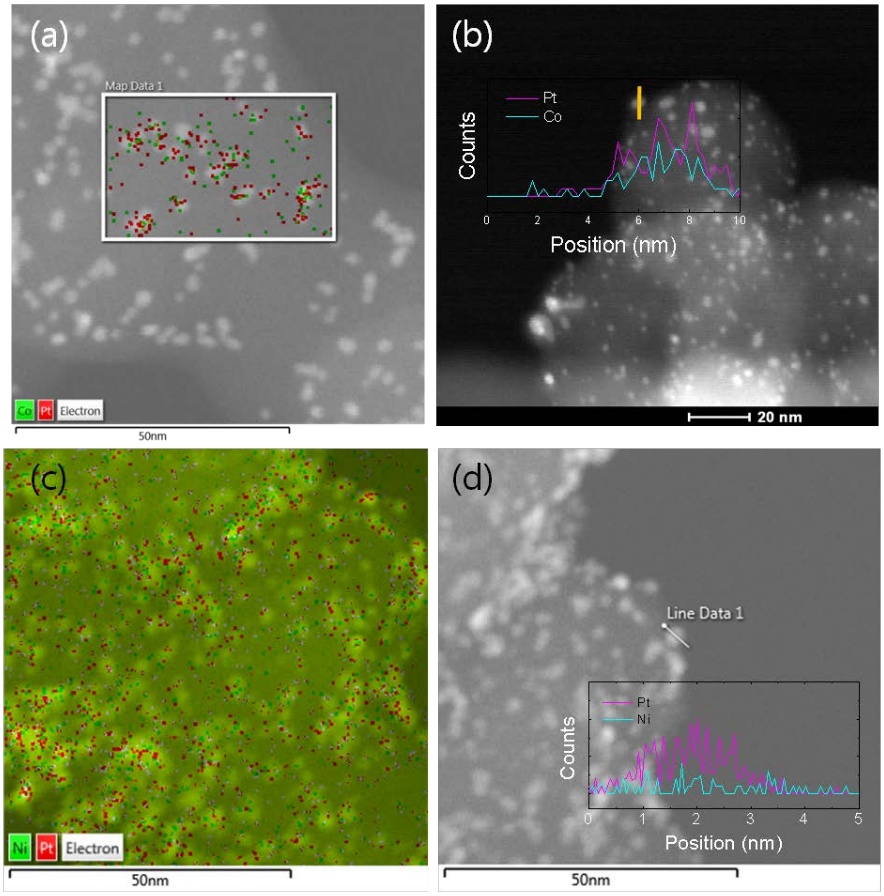

Figure 3. 23 STEM EDS (a) mapping and (b) line scan data of PtCo/C, (c) mapping and (d) line scan data of PtNi/C

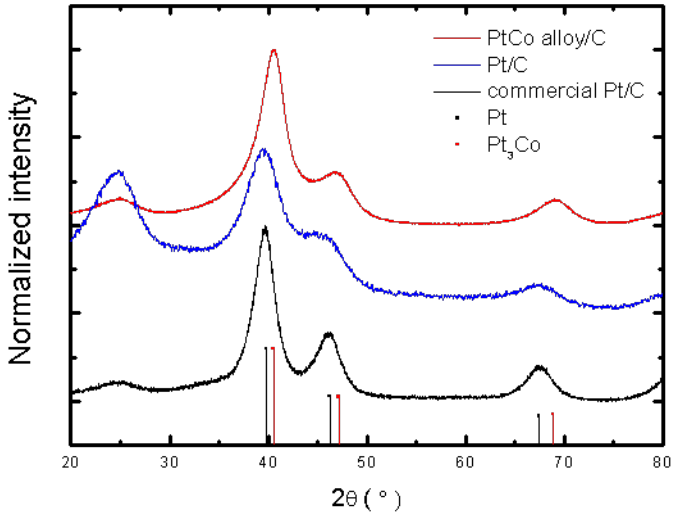

Figure 3. 24 XRD diffraction patterns of PtCo/C and PtNi/C

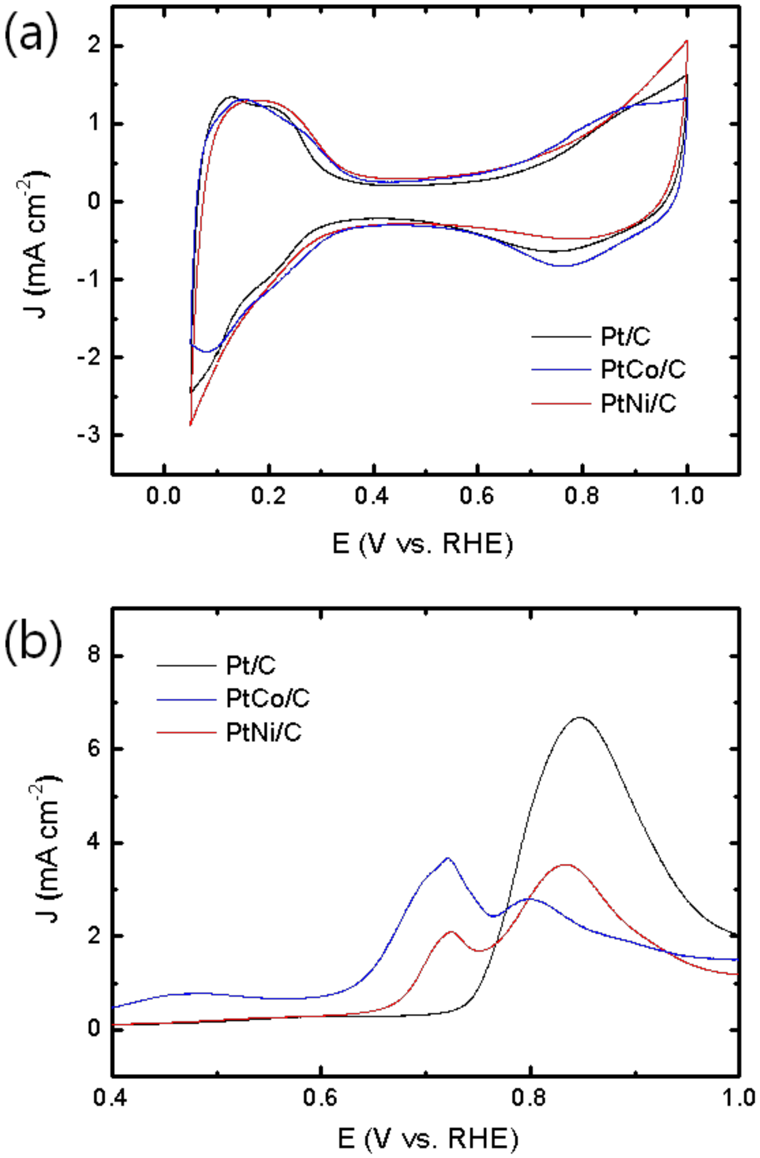

Figure 3. 25 (a) Cyclic voltammograms and (b) CO stripping curves of PtCo/C and PtNi/C

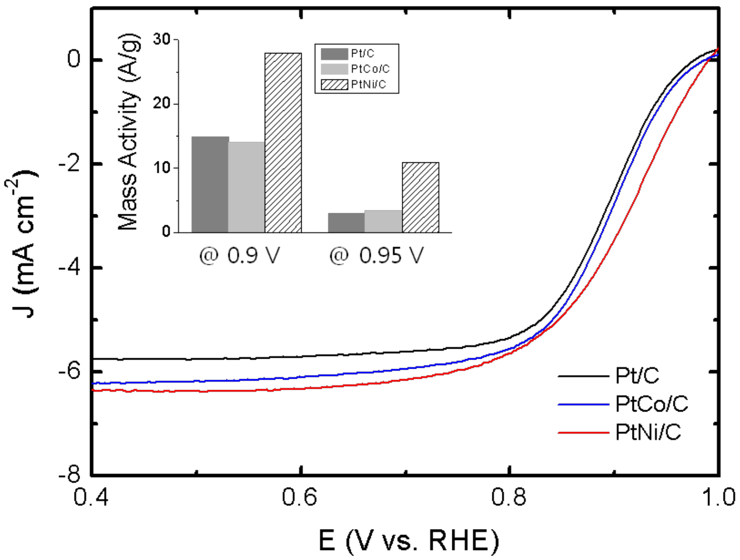

Figure 3. 26 ORR polarization curves from PtCo/C and PtNi/C (inset : mass activities)

\

	Pt/C	PtCo/C	PtNi/C
ECSA (m^2/g_{Pt})	51.0	34.6	44.3
Half-wave potential	0.890	0.892	0.907
Mass activity at 0.9 V	14.8	14.0	27.9
Mass activity at 0.95 V	2.99	3.38	10.9

Table 3. 2 ORR activity indexes

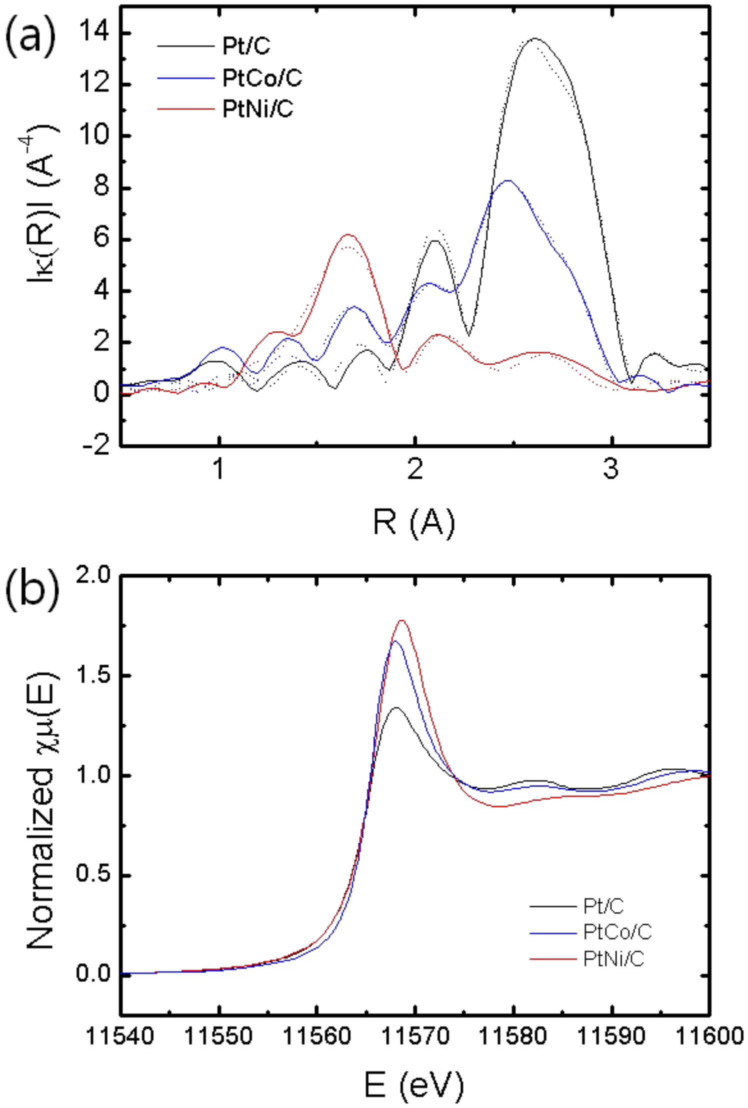

Figure 3. 27 (a) EXAFS spectra and (b) Pt L3 edge XANES spectra

	Pt-Pt		Pt-M		Pt-O	
	r (Å)	n	r (Å)	n	r (Å)	n
Pt/C	2.76	11.3				
PtCo/C	2.71	6.4	2.64	2.3	2.2	2.1
PtNi/C	2.66	3.5	2.41	1.2	2.2	4

Table 3. 3 Atomic distances and coordination numbers estimated from EXAFS fitting

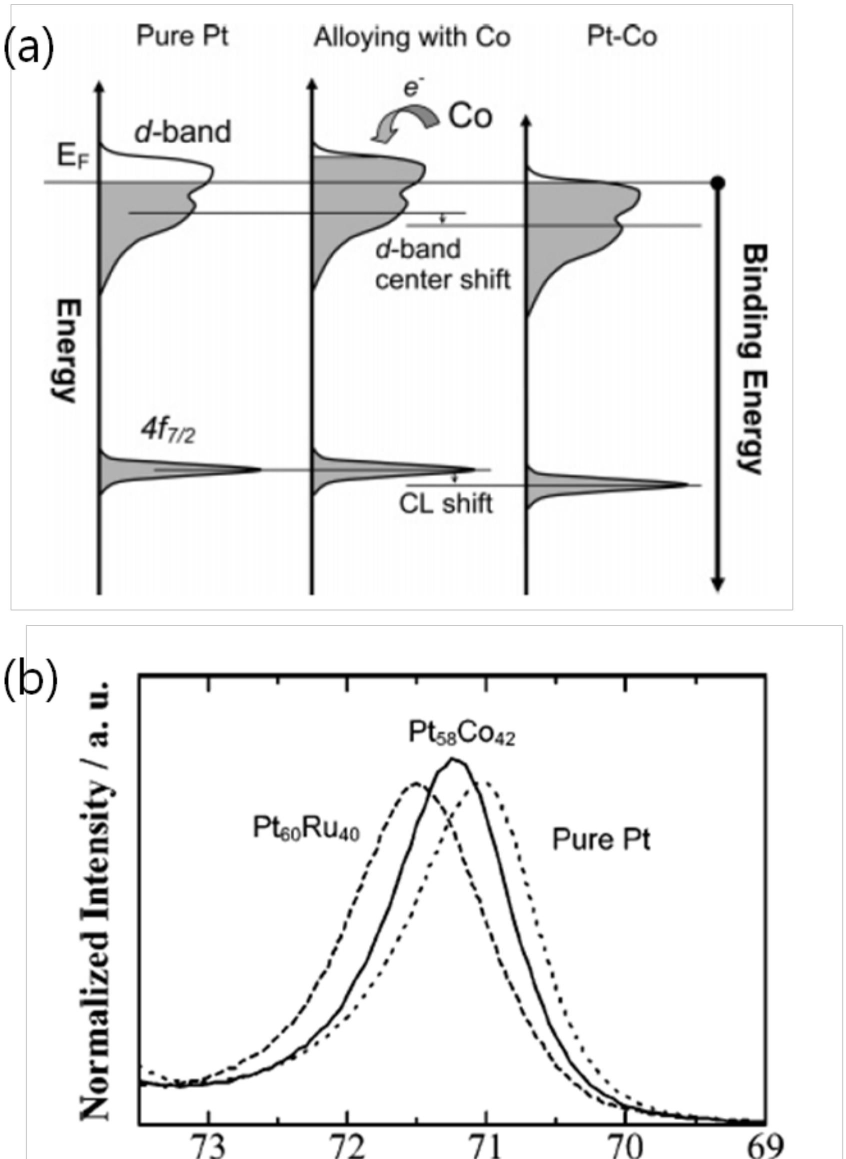

Figure 3. 28 (a) Schematic explanation of the alloying effect on the electronic structures of Pt, (b) core level spectra of Pt 4f for pure Pt and Pt alloy

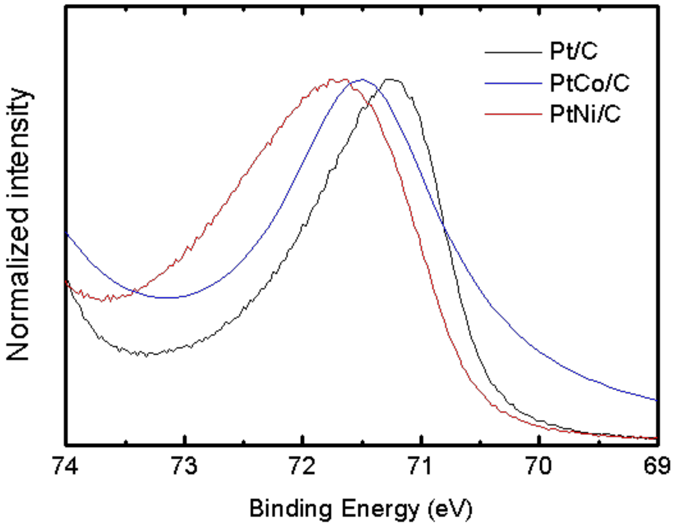

Figure 3. 29 Pt 4f XPS spectra of PtCo/C and PtNi/C

3.2.2. Core-shell nanoparticles via microwave associated 2-step method

Cobalt-platinum core-shell structured nanoparticles were synthesized via modified liquid sputtering method. First, cobalt seed material was prepared by liquid sputtering, and then microwave assisted shell reduction was conducted with injected precursor of platinum shell material. [30] Precursor ions are distributed around cobalt core nanoparticle due to ionic interactions and reduced on the core metal surface by energy transferred from microwave irradiation. Carbon supports were added when synthesis was completed in order to prevent precursor reduction on support surface instead of core surface. As well as section 3.2.1, supporting was carried through one hour sonication and overnight stirring.

Amount of platinum precursor was varied from 10 mg to 30 mg in order to alter shell thickness. 2-3 nm sized core-shell nanoparticles were successively prepared with this procedure and it is hard to find well defined core-shell structure in this size range. Extremely small sized core-shell structure fabrication was possible since surface oxide formation was suppressed via vacuum synthesis.

Figure 3.30 shows HRTEM images of synthesized nanoparticles. Spherical shaped metal NPs were well distributed on carbon supports with a narrow size distribution. Average diameters were 2.02 ± 0.40 nm, 2.36 ± 0.59 nm and 2.54 ± 0.81 nm for PtCo10/C, PtCo20/C and PtCo30/C, respectively. The reduction of platinum precursor on cobalt surface was confirmed through increased average particle size as amount of injected platinum precursor increased. Additional platinum reduction experiment was conducted without cobalt seed. 6.5 wt. % of Pt/C was synthesized with 20 mg of platinum precursor; 14 % of platinum yield. CoPt20, synthesized under same condition has a 24 wt. % and 57 % of platinum yield. Thus, cobalt nanoparticle in this experiment acts as both seed and platinum reduction catalyst and preferential reduction of platinum on cobalt surface is predicted.

Phase structures of synthesized nanoparticles were investigated using X-ray diffraction patterns in figure 3.32. In case of CoPt10 sample, platinum diffraction peaks were disappeared, while cobalt and cobalt oxide diffraction peaks clearly observed. It is estimated that injected amount of platinum precursor was not sufficient to be detected with diffraction peaks and cover cobalt nanoparticle surface completely with platinum shell. Therefore, surface exposed cobalt atoms were oxidized to cobalt oxide.

Whereas, separated platinum and cobalt diffraction peaks were observed and cobalt oxide peaks were vanished in CoPt20 sample; platinum diffraction peaks have low intensity because platinum shell is thin and cobalt diffraction peaks are slightly down shifted due to expansion strain of platinum shell. It is expected that completely covered cobalt-platinum core-shell structures were successively synthesized. In order to prove core-shell structure, additional heat treatment was carried out under hydrogen atmosphere at 160 ℃. Because cobalt has larger hydrogen adsorption binding energy than platinum

[31], cobalt will emerge out to surface and form alloy with platinum if cobalt presents in core part as desired. Whereas platinum and cobalt nanoparticles are exist separately, no diffraction pattern change will be observed since 160 ℃ is not sufficient to induce segregation of supported nanoparticles. Experimental results confirm the high angle shift of platinum diffraction peaks which clearly means alloy formation and reduction of cobalt diffraction peak intensity.

From the obtained CoPt30 XRD pattern, alloy structure was conformed instead of core-shell structure. During platinum reduction reaction on cobalt surface, some replacement reaction between cobalt and platinum is expected due to more negative reduction potential of cobalt than platinum. It is supposed that replacement reaction occurred actively by the excess amount of platinum precursor. Measure (2 2 0) diffraction peak was 68.3 ° and lattice parameter at this position referred to 3.88 Å. Since it is located between indexed Pt and Pt_3Co composition, the composition of CoPt30 was calculated using Vegard’s low on the basis of the two indexed composition; estimated composition was Pt_6Co.

STEM EDS analysis was conducted to reaffirm core-shell structure. In all prepared samples, EDS mapping results clearly show co-existence of two elements in one particle in figure 3.33 for CoPt10, CoPt20 and CoPt30, respectively. Detected ratio of platinum versus cobalt for each sample was 1.78: 1, 2.85:1 and 5.41:1 for CoPt10, CoPt20 and CoPt30, respectively. The detected composition of CoPt30 is well agreed with XRD study. Line scan images are also shown in figures. Line scan result of figure 3.33 also supports possibility of core-shell structure.

CoPt20 sample was further investigated with high magnitude HRTEM in order to find more evidences of core-shell structure. Figure 3.34 shows obtained fast Fourier transform (FFT) diffraction pattern at one selected particle which is split into two points and inverse Fourier transformation images after masking. The atomic distances obtained from inverse Fourier transformed images are correlated with platinum and cobalt planes.

Average particle size of cobalt seed was estimated for further quantitative analysis. Although direct measuring from HRTEM images of as-prepared cobalt nanoparticles is the best way, it is not easy to obtain clear HRTEM image of non-treated as-prepared cobalt nanoparticles duo to their amorphous phase. Therefore, average particle sized was inversely estimated from size of Co_3O_4 nanoparticle on N2299 support which has the smallest particle size among three different supports used in section 3.2.2. 1.98-fold volume expansion occurs when cobalt is oxidized to cobalt oxide and it is converted to 1.26-fold diameter expansion; 1.85 nm of seed cobalt nanoparticle size was derived from 2.3 nm sized cobalt oxide nanoparticle.

Size of the spherical core-shell particles can be estimated by the following equation where n_{shell}/n_{core} is the number ratio in core-shell structure and V_{shell}/V_{core} is the volume ratio of each atom; [32]

$$d_{shell\,^\wedge core} = [\left(\frac{n_{shell}}{n_{core}}\right)\left(\frac{V_{shell}}{V_{core}}\right) + 1]^{\frac{1}{3}} d_{core}$$

Atomic ratio of platinum versus cobalt was calculated to 1.78, 2.85 and 5.41 by STEM EDS analysis for PtCo10, PtCo20 and PtCo30, respectively. Desired particle size of core-shell structure was calculated to 2.89 nm, 3.27 nm and 3.92 nm using atomic ratio, estimated seed size and atomic radius of platinum (177 pm) and cobalt (152 pm). Particle size was over estimated compared to HRTEM measured particle size due to replacement reaction at cobalt surface was not considered. Conversely, core particle diameter was estimated from whole particle size by HRTEM images; 1.66 nm, 1.56 nm and 1.30 nm for PtCo10, PtCo20 and PtCo30, respectively. Core diameter was linearly decreased with composition (figure 3.35). In particular, increased diameter of 0.8 nm for CoPt20 suggests 0.4 nm of deposited platinum layer. It is equivalent to 1.1 layers; diameter of a platinum atom is 0.36 nm. [32] In same manner, CoPt10 has 0.5 monoatomic platinum layers and PtCo30 has 1.7 layers. (CoPt30 is not core-shell structured particle, it is theoretically calculated value using atomic ratio.)

Electrochemical analysis was conducted for CoPt10 and CoPt20, except CoPt30 which does not have core-shell structure. Commercial 20 wt. % Pt/C was used for control catalyst, since CoPt10 and CoPt20 has weight percent of 20 and 24, respectively. Strain effect and modified electronic structure induced by core material leads to H_{upd} peak shape change and earlier CO oxidation likewise 3.3.1. CoPt20 showed the resulting increase in ORR performance, but CoPt10 exhibited rather inferior performance due to lack of platinum loading. In addition, reduction of platinum amount causes mass activity increment. ECSA, half wave potential and mass activity are listed in table 3.4.

For further insight into the electronic structures of core-shell catalysts, XAFS measurements were carried out. Calculated atomic distances and coordination numbers from fitted extended X-ray absorption fine structure (EXAFS) data are listed in Table 3.5. Data and fits of the magnitude of Fourier transformed k3-weighted EXAFS spectra are shown in figure 3.38 (a). It was revealed that CoPt10 forms island structure instead of core-shell due to lack of platinum precursor and coordination number form EXAFS data showed same trend; coordination number of Pt-Pt was decreased and Pt-Co was increased compared to CoPt20. Also, more reduced atomic distance proves higher strain effect from cobalt core. At the Pt L3 edge (figure 3.38 (b)), white line intensity of CoPt10 and CoPt20 are slightly higher than control platinum sample. This small variation indicated the hybridization of platinum with cobalt. [33]

Core-shell like nanoparticles were synthesized via microwave assisted liquid sputtering method, and core-shell formation was confirmed by various techniques such as STEM EDS, XRD, HRTEM FFT patterns and XAFS. Core-shell induced ORR performance enhancement was also measured.

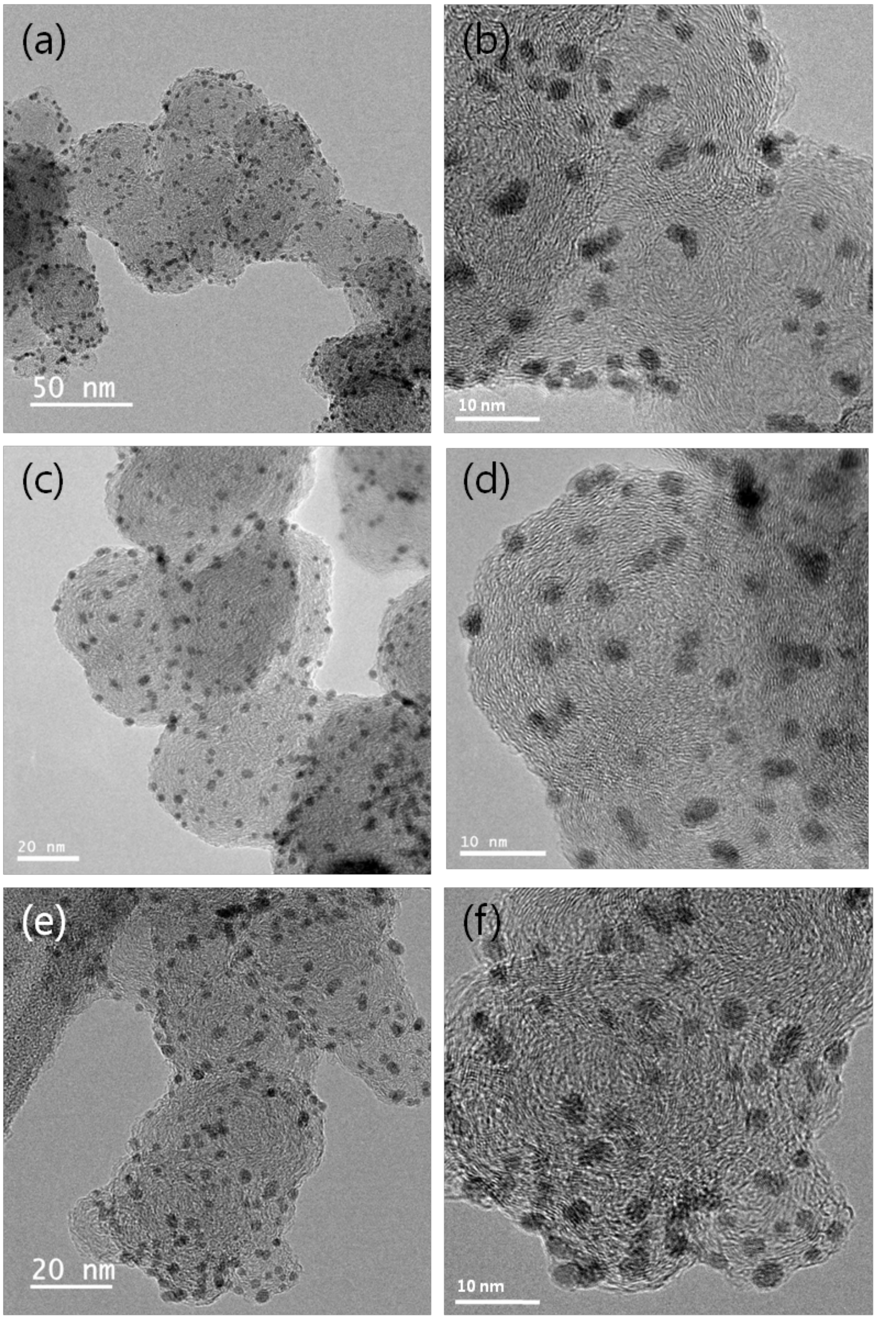

Figure 3. 30 HRTEM images of (a), (b) CoPt10, (c), (d) CoPt20 and (e), (f) CoPt30

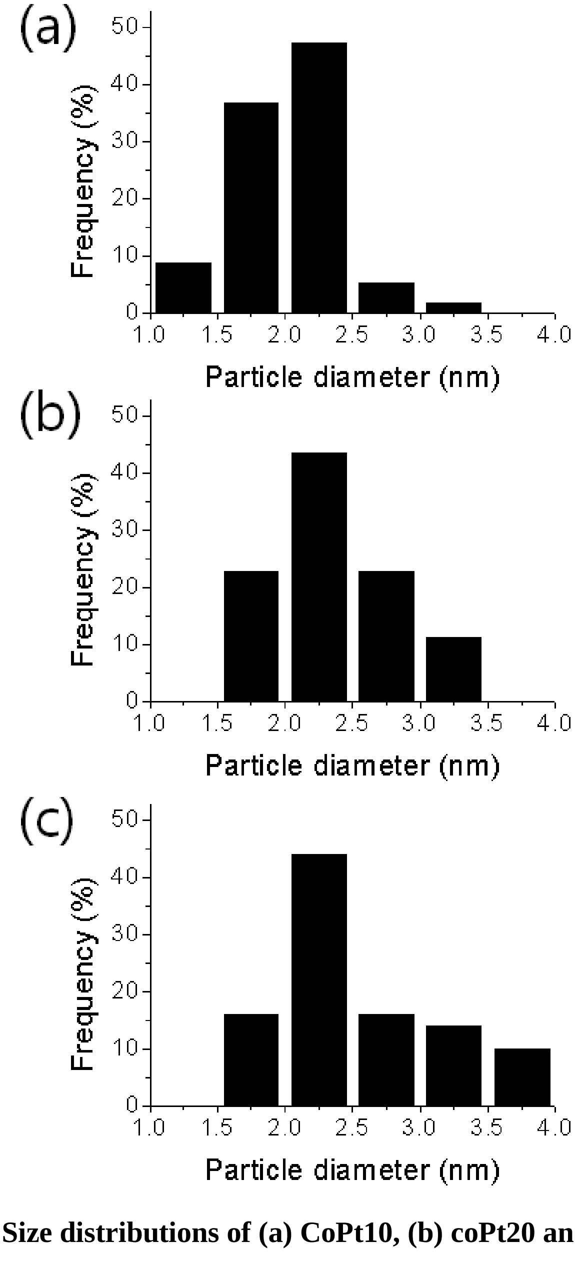

Figure 3. 31 Size distributions of (a) CoPt10, (b) coPt20 and (c) CoPt30

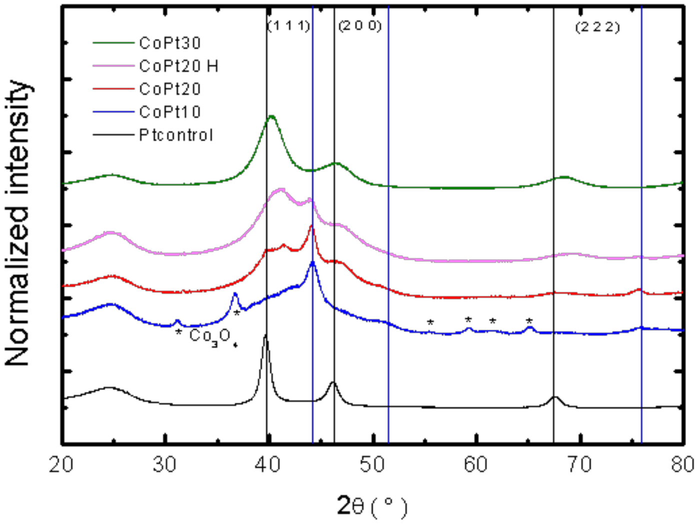

Figure 3. 32 XRD diffraction patterns of CoPt10, CoPt20 and CoPt30

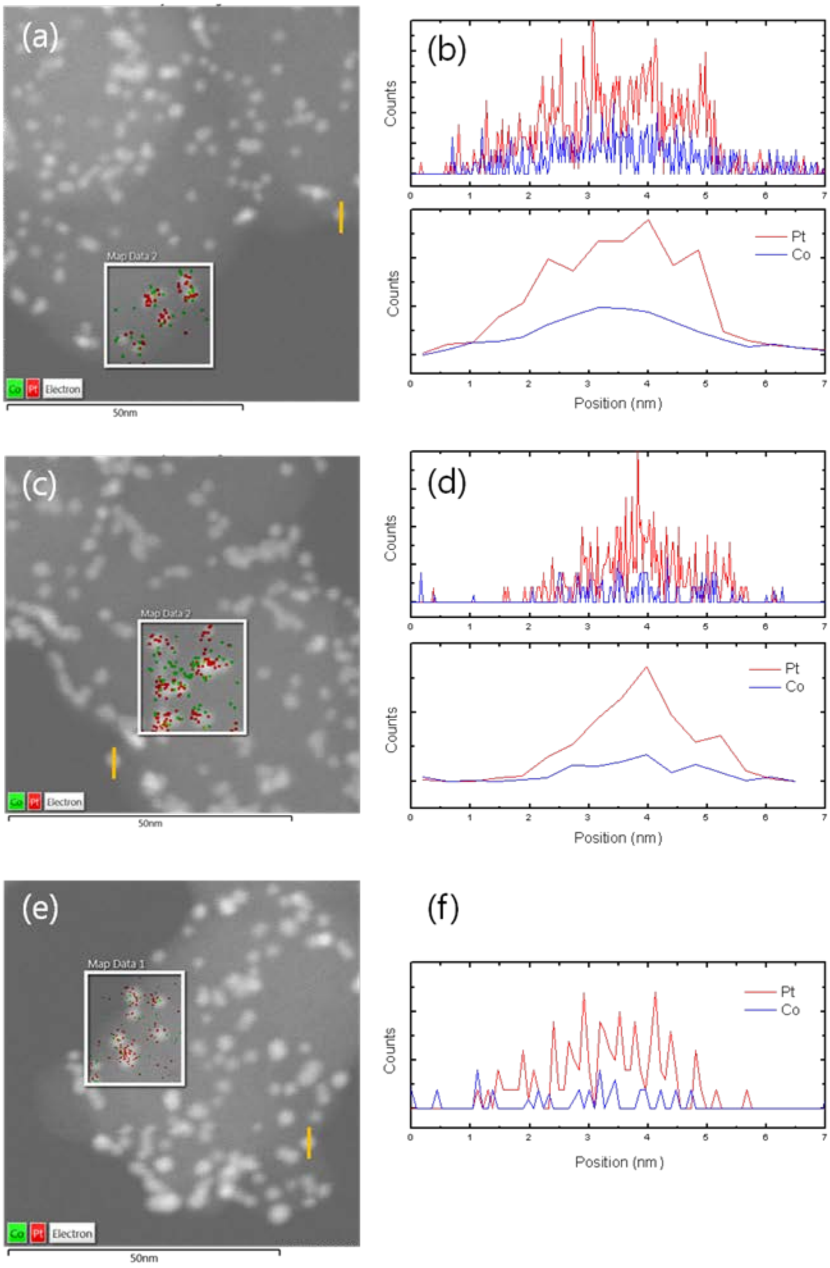

Figure 3. 33 STEM EDS (a), (c), (e) mappings and (b), (d), (f) line scan data for PtCo10, PtCo20 and PtCo30

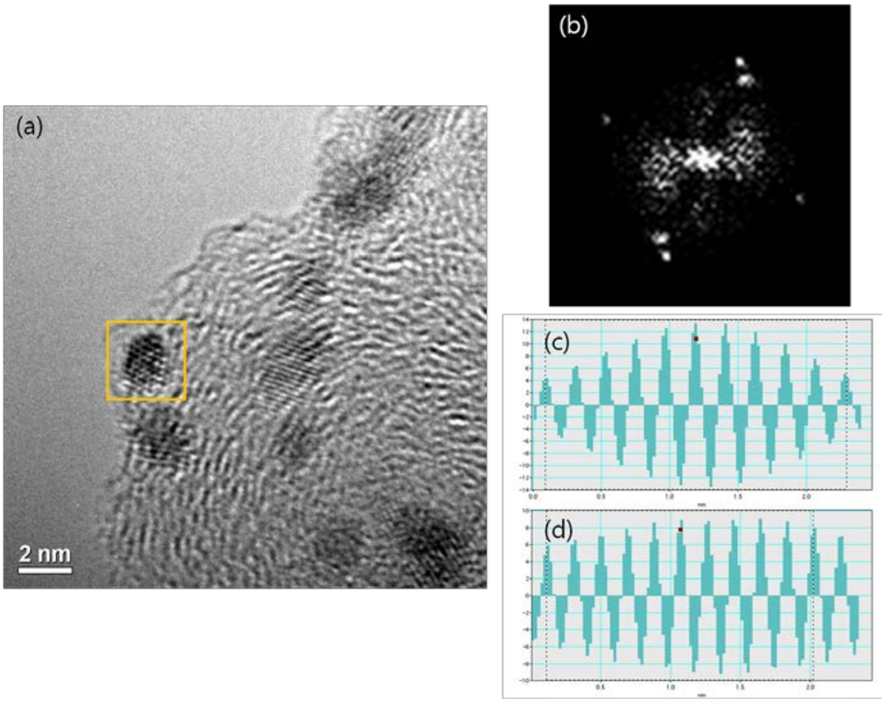

Figure 3. 34 (a) High magnitude HRTEM image, (b) FFT pattern and (c) and (d) inversed FFT patterns of CoPt20

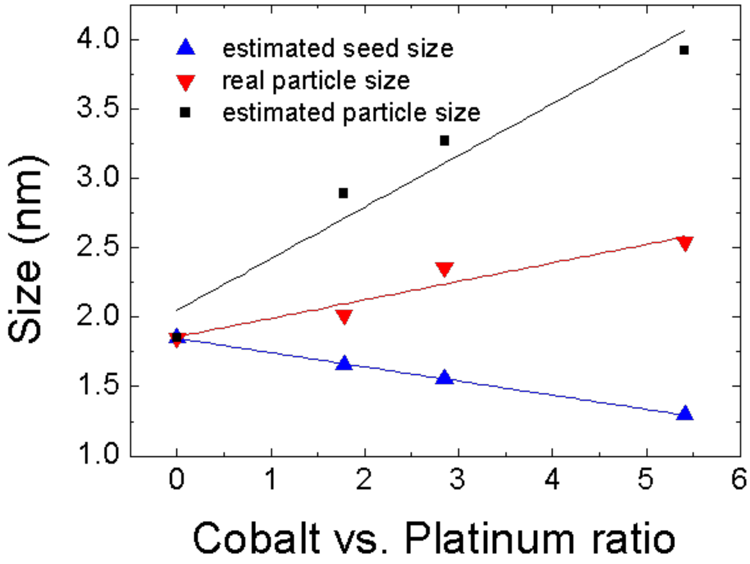

Figure 3. 35 Correlation between composition and seed size

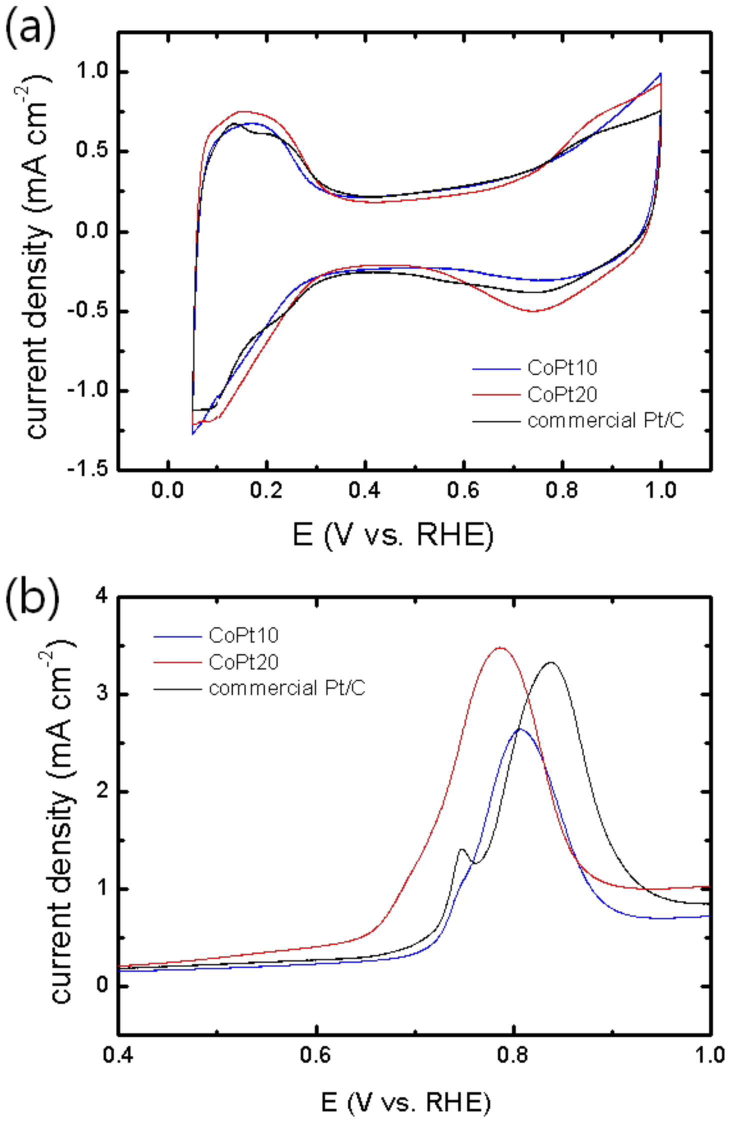

Figure 3. 36 (a) Cyclic voltammograms and (b) CO stripping curves of CoPt10 and CoPt20

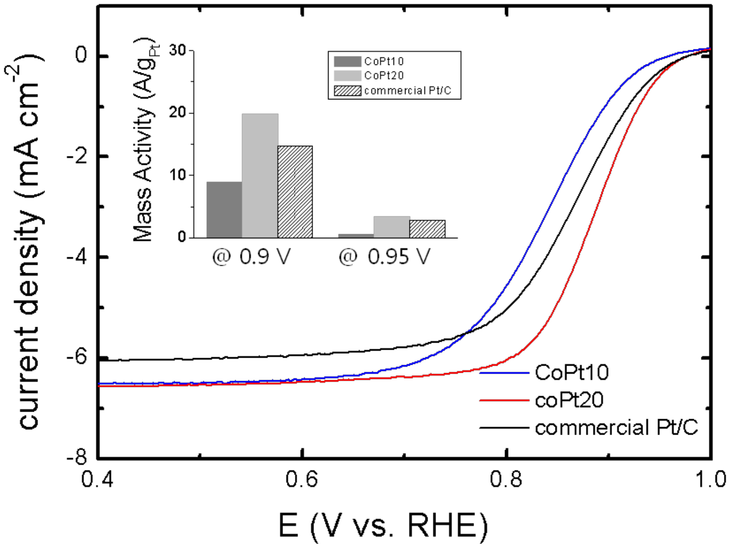

Figure 3. 37 ORR polarization curves from CoPt10 and CoPt20 (inset : mass activities)

	CoPt10	CoPt20	Commercial Pt/C
ECSA (m^2/g_{Pt})	45.9	36.0	33.4
Half-wave potential	0.83	0.88	0.86
Mass activity at 0.9 V	8.9	19.9	14.8
Mass activity at 0.95 V	0.6	3.4	2.8

Table 3. 4 ORR activity indexes

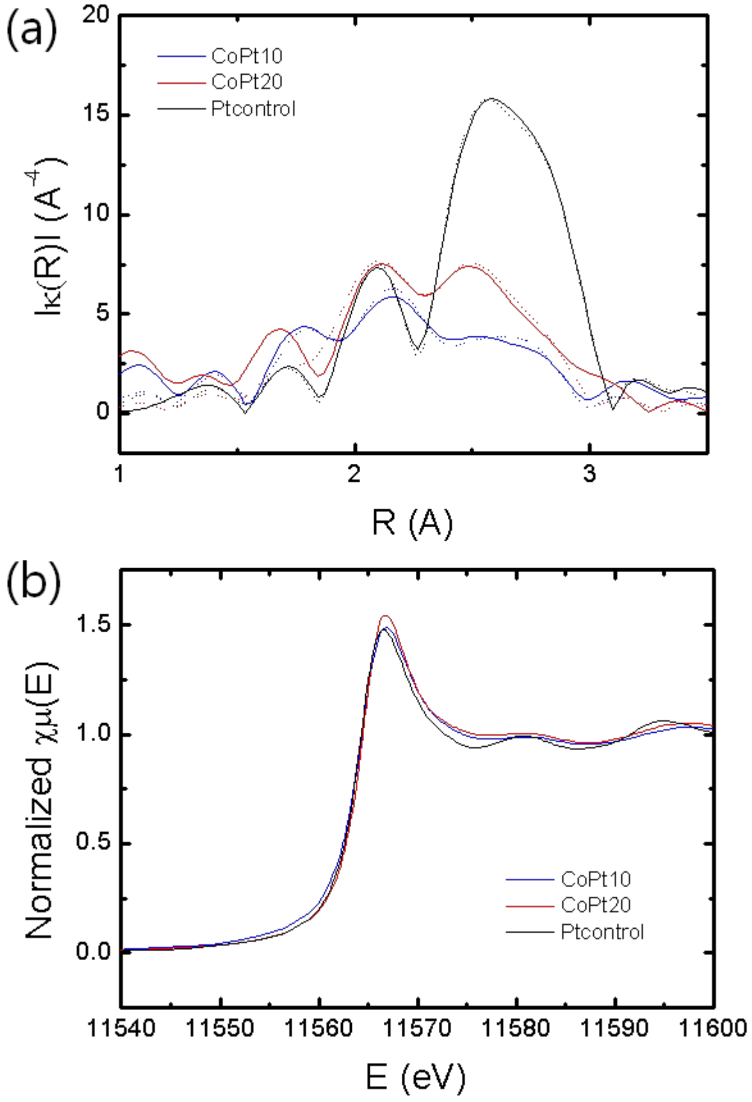

Figure 3. 38 (a) EXAFS spectra and (b) Pt L3 edge XANES spectra

	Pt-Pt		Pt-Co		Pt-O	
	r (Å)	n	r (Å)	n	r (Å)	n
CoPt10	2.70	5.15	2.54	3.80	2.13	0.01
CoPt20	2.72	7.5	2.59	3.25	2.16	0.16
Pt control	2.75	12				

Table 3. 5 Atomic distances and coordination numbers estimated from EXAFS fitting

3.2.3. Co oxide/C electrocatalyst

The scarcity of platinum metal causes economical restrictions to use large amount of platinum as catalyst, despite of superior oxygen reduction activity of platinum. Various method to minimize the amount of platinum has been proposed, the best solution is find the other materials to completely replace the platinum. Complete replacement of platinum in acidic media is still difficult, it was recently reported that some spinels and perovskites have comparable oxygen reduction activities in alkaline media.

Moreover, cobalt oxides have shown considerable catalytic activities toward oxygen evolution reaction (OER). Combining oxygen evolution and reduction activities, continuous use of renewable energy through bi-functional catalyst is possible. Cobalt is also advantageous in terms of price, compared with iridium or ruthenium, which reported to have high OER activities but insufficient reserves. However, causticity and low conductivity still remains to be improved.

In this chapter, cobalt oxide nanoparticles were synthesized via liquid sputtering method and adopted as oxygen reduction and oxygen evolution bi-functional catalyst in alkaline media. It was confirmed that ionic liquid synthesis is not suitable for practical catalyst synthesis in the previous chapter, only PEG solvent experiments were conducted.

Cobalt nanoparticles were synthesized on various carbon supports (VC, untreated CNT and N2299) using PEG solvent and transformed to cobalt oxide nanoparticles by 250 ℃ heat treatment under air atmosphere. Acid treatment of CNT, in order to introduce functional groups, has advantages on dispersion into solvent and evenly distributed metal nanoparticle synthesis, while surface corrosion is progressed and electric conductivity is lowed by disrupting the hybridized sp^2 carbon network structure. [34] Therefore, untreated CNT is used for bi-functional catalyst, since bi-functional catalyst covers wider voltage range.

HRTEM (figure 3.39) shows that nano-sized cobalt oxide particles were fabricated on supports, at the same time aggregation of nanoparticles due to the magnetic properties of cobalt is also confirmed. [35] Synthesis of well dispersed cobalt nanoparticle requires a lot of effort due to the collective behavior of magnetic cobalt nanoparticles. To obtain evenly distributed cobalt oxide nanoparticles, synthetic method was modified. Cobalt sputtering was conducted onto PEG solvent without supports. Carbon supports were injected after Co nanoparticle containing PEG solvent was diluted with EG solution (PEG: EG=1:3, volumetric ratio). Sonication and overnight stirring was carried to strengthen interaction between metal nanoparticles and supports. [36] Although more steps were added and longer time was required than aforementioned method, a much improved dispersion of the particles were confirmed through HRTEM image. Nanoparticles had average size of 3.0 ± 1.2 nm, 3.2 ± 1.3 nm and 2.3 ± 0.6 nm for Co_3O_4/VC, Co_3O_4/CNT and Co_3O_4/N2299, respectively.

The crystallinity of samples was investigated by obtained XRD patterns.

Figure 3.41 and figure 3.42 shows XRD patterns of each sample before and after modified experiments. Diffraction peaks at 31.2 °, 36.8 °, 44.8 °, 55.7 °, 59.4 ° and 65.2 ° of 2Θ refer to (2 2 0), (3 1 1), (4 0 0), (4 2 2), (5 1 1) and (4 4 0) planes of cubic phase Co_3O_4 (JCPDS file no. 43-1003), respectively. An additional broad peak at 2Θ of 20-30 ° is originated from carbon support. Although intensity of diffraction peak was decreased after experimental procedure was modified, synthesis of single Co_3O_4 phase was confirmed regardless of the conditions.

The ORR catalytic activity was investigated by RDE in O_2 saturated 0.1 M KOH solution. Figure 3.43 shows oxygen reduction polarization curves of Co_3O_4/VC, Co_3O_4/CNT, Co_3O_4/N2299, modified Co_3O_4/VC, Co_3O_4/CNT and Co_3O_4/N2299 samples. The half wave potential, the potential where the current is half of limiting current, and onset potential, the potential where the cathodic current attained to 20 μA/cm^2, were adopted for indicator of the high ORR activity and illustrated in figure 3.44. All distribution improved samples exhibited better catalytic activities and half wave potentials were shifted toward positive directions about 20 – 40 mV, although cobalt oxide loading amount was reduced from 50 wt. % to 15 wt. %. In other words, cobalt oxides were more efficiently utilized on well dispersed samples. Moreover, as reported in previous papers, synergetic effect of the graphene-Co_3O_4 composite [37] for ORR activity was reaffirmed by positive potential and higher current density of N2299 sample; half wave potential of 0.79 V was obtained, the value is comparable to recently reported papers on graphene-Co_3O_4 composites. [38]

To clarify ORR kinetics in graphene-Co_3O_4 composites, linear sweep voltammograms at various rotating speeds were obtained in O_2 saturated 0.1 M KOH solution. Figure 3.45 (a) confirmed that limiting current increases as angular velocity increases. Using Koutecky-Levich equation, the number of electrons involving ORR can be calculated as follows; [38]

$$\frac{1}{j} = \frac{1}{j_k} + \frac{1}{B\omega^{\frac{1}{2}}}$$

$$B = 0.62nFC_{O_2}D_{O_2}^{\frac{2}{3}}\nu^{\frac{-1}{6}}$$

j = measured current

j_k = kinetic current in the absence of mass transfer effect

ω = rotating speed

n = number of electrons involved per oxygen molecule

F = Faraday constant, 96485 C

C_{O2} = bulk concentration of O_2, 1.2×10^{-6} mol cm^{-3}

D_{O2} = diffusion coefficient of O_2 in 0.1 M KOH solution, 1.9×10^{-5} cm^2 s^{-1}

ν = kinetic viscosity, 0.01 cm^2 s^{-1}

Koutecky-Levich slope was obtained by plotting reciprocal current as a function of the inverse of the square root of the angular velocity at various potential points (figure 3.45 (b)). The linearity and near parallelism of K-L plots at different potential from 0.3 V to 0.7 V suggests first order reaction kinetics toward the concentration of dissolved oxygen and similar electron transfer at different potentials. [37] In fact, estimated electron transfer numbers from K-L equation had similar values in the range of 3.51 to 3.98, which indicated four-electron process is predominant in graphene-Co_3O_4 composite sample.

OER catalytic activity was also examined by cyclic voltammograms in O_2 saturated 0.1 M KOH solution. Solid lines of figure 3.46 (a) show collected voltammograms after capacitive correction and dotted lines exhibit voltammograms after ohmic drop (iR) correction on capacitive corrected current. Capacitive correction was carried by averaging forward and backward current and ohmic electrolyte resistance of 45 Ω was adopted for iR compensation. [39]

Co_3O_4/N2299 shown highest catalytic activity likewise ORR, increment is not significant when comparing to CNT. However, measured potential at current density of 1.5 mA cm^{-2} was very promising with fairly positive values; 1.60 V, 1.60 V and 1.63 V for Co_3O_4/N2299, Co_3O_4/CNT and Co_3O_4/VC, respectively for capacitive corrected current. Tafel plots were derived using capacitive and iR corrected current and shown in figure 3.46 (b). Tafel slope of Co_3O_4/N2299 downed to 67.2 mV/decade and proved Co_3O_4/N2299 sample has considerable activities on both ORR and OER; Small Tafel slope implys efficient catalyst for OER. 70.5 mV/decade and 86.2 mV/decade of

Tafel slope was recorded for Co_3O_4/CNT and Co_3O_4/VC respectively. Theoretically, 60 mV/decade of Tafel slope means rate-determining step for oxygen gas evolution on either oxide is an activation-controlled process involving one electron transfer, and Co_3O_4/N2299 and Co_3O_4/CNT are expected to in the range of this process. [40]

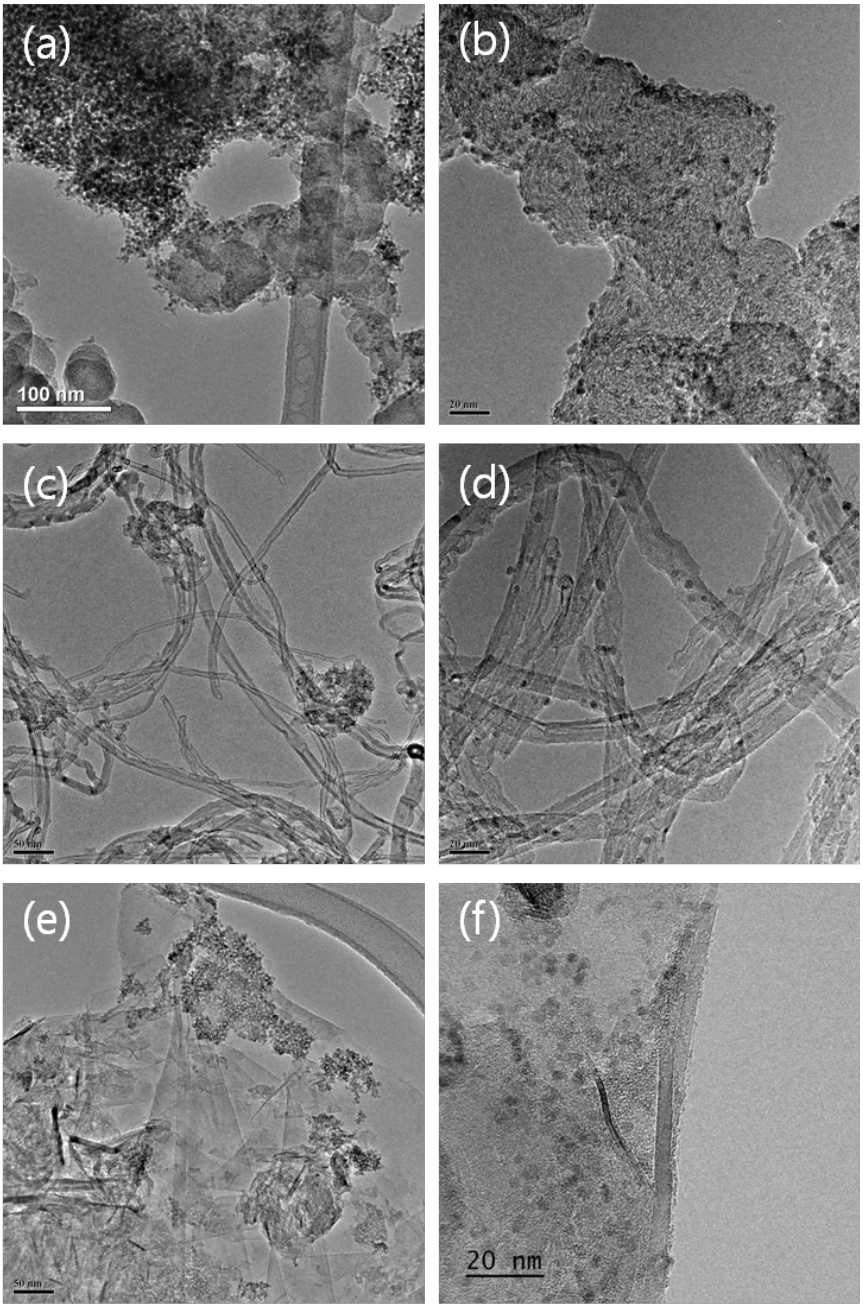

Figure 3. 39 HRTEM images of Co3O4 on (a), (b) VC, (c), (d) CNT and (e), (f) N2299 (a, c, e : before modification, b, d, f : after modification)

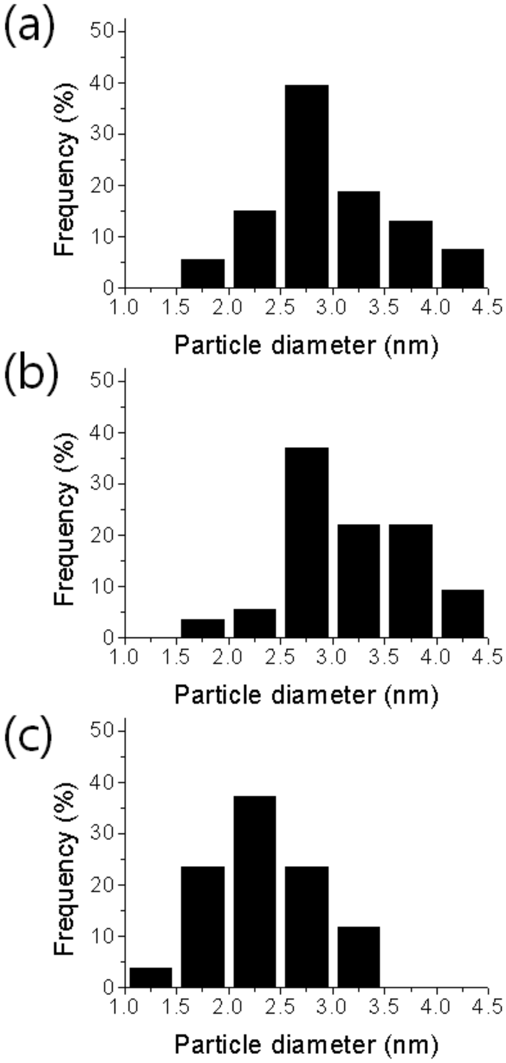

Figure 3. 40 Size distributions of (a) VC, (b) CNT and (c) N2299

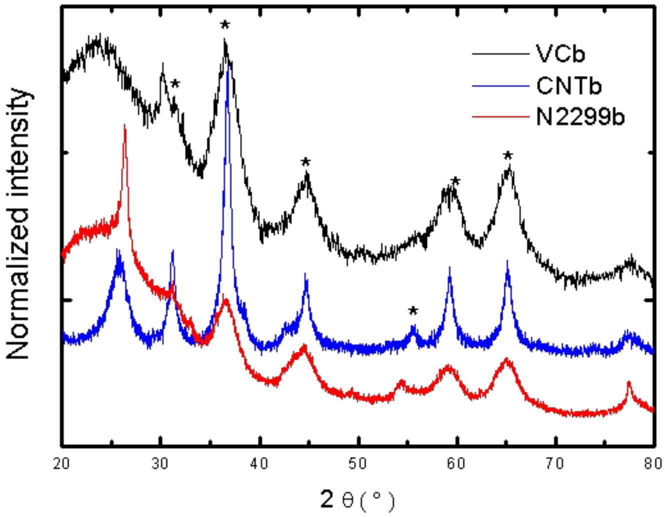

Figure 3. 41 XRD diffraction patterns from agglomerated cobalt oxides

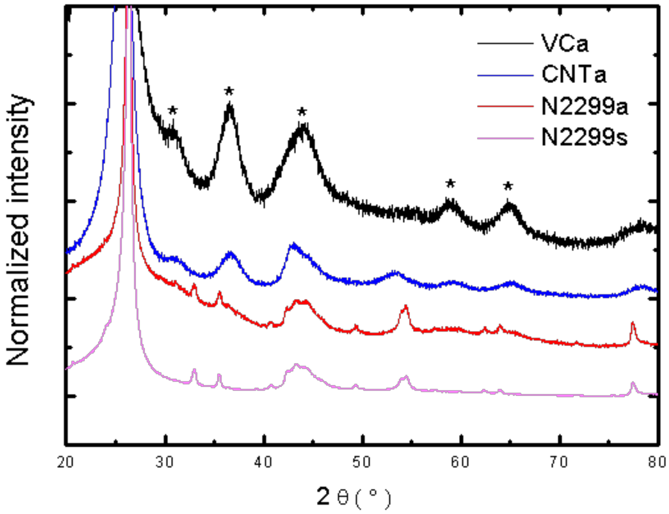

Figure 3. 42 XRD diffraction patterns from well dispersed cobalt oxides

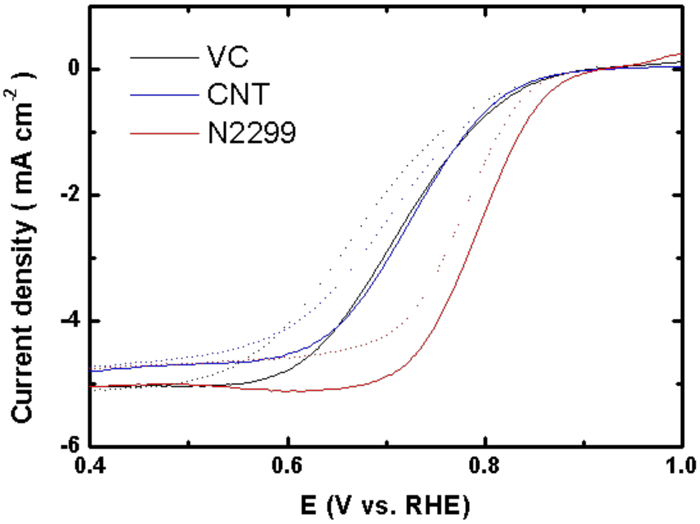

Figure 3. 43 ORR polarization curves of cobalt oxides

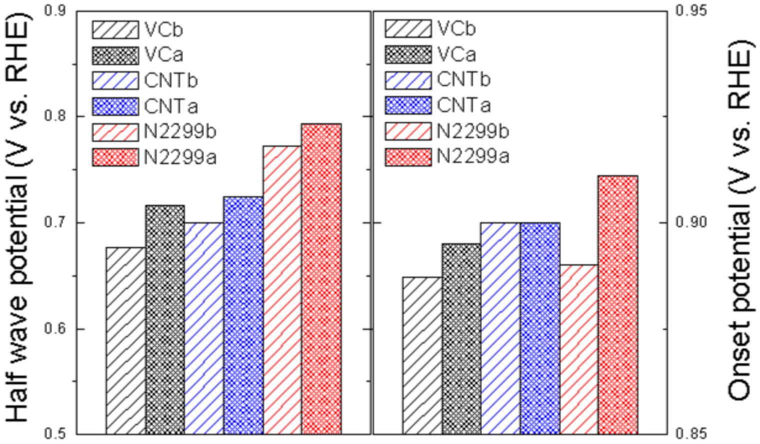

Figure 3. 44 Half wave potentials and onset potentials from cobalt oxides

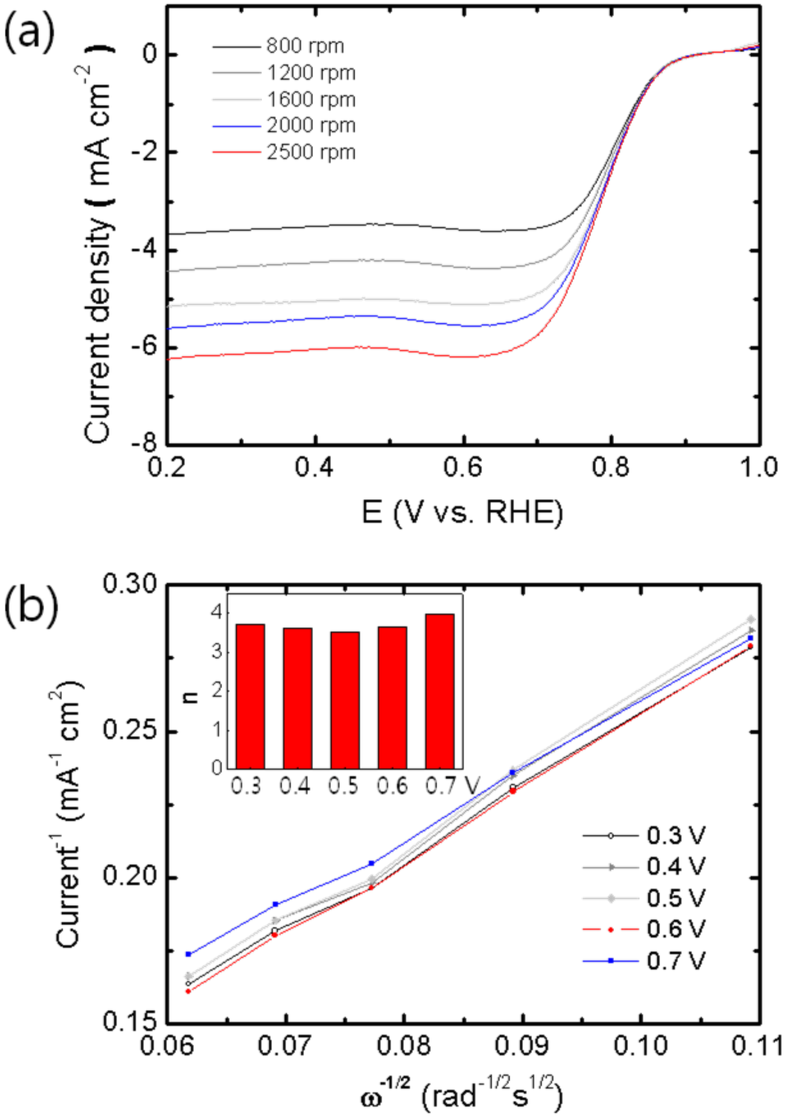

Figure 3. 45 (a) ORR polarization curves from various rpm and (b) Koutecky-Levich plot (inset : calculated electron transfet number)

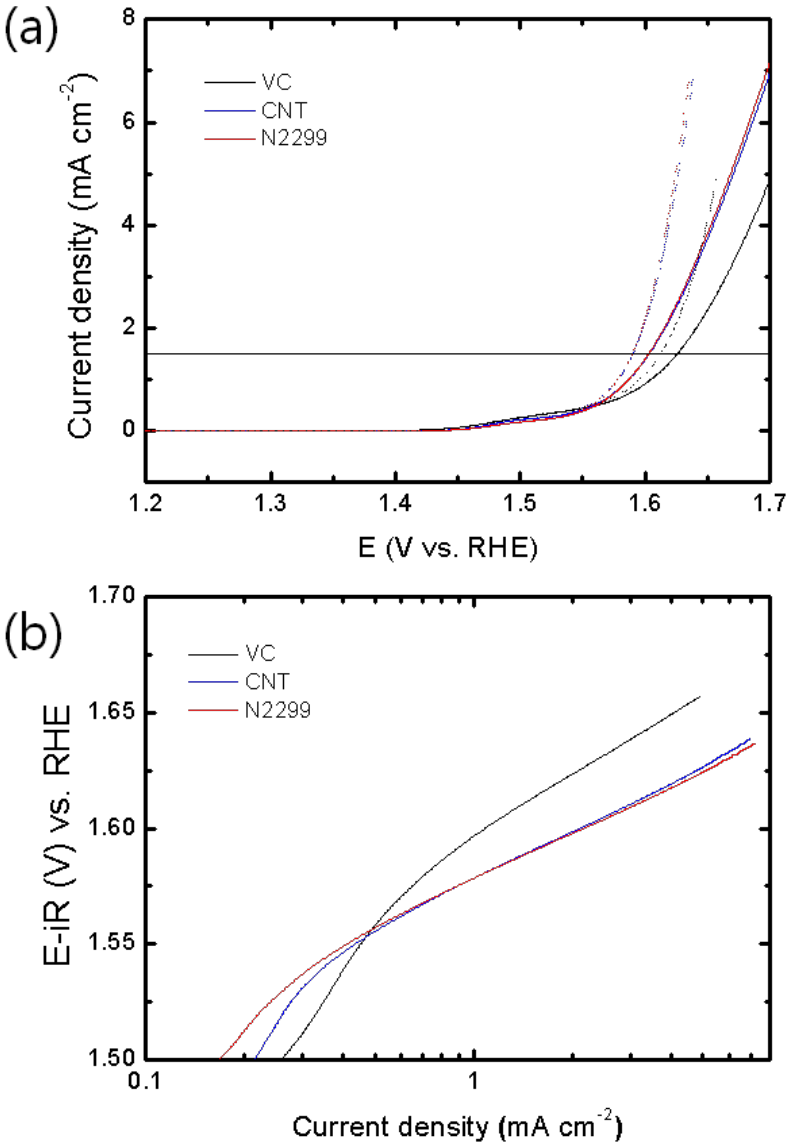

Figure 3. 46 (a) OER polarization curves and (b) Tafel plots from cobalt oxides

3.3. References

[1] O. P. Khatri, K. Adachi, K. Murase, K. Okazaki, T. Torimoto, N. Tanaka, S. Kuwabata and H. Sugimura, "Self-Assembly of Ionic Liquid (BMI-PF6)-Stabilized Gold Nanoparticles on a Silicon Surface: Chemical and Structural Aspects", *Langmuir*, **2008**, 24, 7785–7792.

[2] K. Okazaki, T. Kiyama, T. Suzuki, S. Kuwabata and T. Torimoto, "Thermally Induced Self-assembly of Gold Nanoparticles Sputter-deposited in Ionic Liquids on Highly Ordered Pyrolytic Graphite Surfaces", *Chem. Lett.*, **2009**, 38, 330-331.

[3] H. G. Oswin and M. A. D. Phill, "Platinum Metals in the Fuel Cell – Their function and applications in electrode structures", *Platinum Metals Rev.*, **1964**, 8, 42-48.

[4] A.W. Chester and E. G. Derouane, Zeolite Characterization and Catalysis: A Tutorial, 2009, Springer

[5] T. Nishida, Y. Tashiro and M. Yamamoto, "Physical and electrochemical properties of 1-alkyl-3-methylimidazolium tetrafluoroborate for electrolyte", *J. Fluorine Chem.*, **2003**, 120, 135-141.

[6] H. Matsumoto, M. Yanagida, K. Tanimoto, M. Nomura, Y. Kitagawa and Y. Miyazaki, "Highly conductive room temperature molten salts based on small trimethylalkylammonium cations and bis (trifluoromethylsulfonyl) imide", *Chem. Lett.*, **2000**, 8, 922-923.

[7] H. Matsumoto, H. Kageyama and Y. Miyazaki, *Molten Salts XIII*, 2002,

Electrochemical Society Series Vol. 19 (The Electrochemical Society, Pennington, NJ), 1057

[8] S. V. Dzyuba and R. A. Bartsch, “Influence of Structural Variations in 1-Alkyl(aralkyl)-3-Methylimidazolium Hexafluorophosphates and Bis(trifluoromethylsulfonyl)imides on Physical Properties of the Ionic Liquids”, *ChemPhysChem,* **2002**, 3, 161-166.

[9] J. G. Huddleston, A. E. Visser, W. M. Reichert, H. D. Willauer, G. A. Broker and R. D. Rogers, “Characterization and comparison of hydrophilic and hydrophobic room temperature ionic liquids incorporating the imidazolium cation”, *Green Chem.,* **2001**, 3, 156-164.

[10] B. Q. Wu, R. G. Reddy and R. D. Rogers, Proc. Solar Forum, Solar Energy: The Power to Choose, Washington, D.C., 2001.

[11] C. Hardacre, J. D. Holbrey, S. P. Katdare and K. R. Seddon, “Alternating copolymerisation of styrene and carbon monoxide in ionic liquids”, *Green Chem.,* **2002**, 4, 143-146.

[12] D. R. MacFarlane, P. Meakin, J. Sun, N. Amini and M. Forsyth, “Pyrrolidinium Imides: A New Family of Molten Salts and Conductive Plastic Crystal Phases”, *J. Phys. Chem. B,* **1999**, 103, 4164-4170.

[13] http://en.solvionic.com

[14] A. M. Fernandes, M. A. A. Rocha, M G. Freire, I. M. Marrucho, J. A. P. Coutinho and L. M. N. B. F. Santos, “Evaluation of Cation-Anion Interaction Strength in Ionic Liquids”, *J. Phys. Chem. B,* **2011**, 115, 4033–4041.

[15] H. Zhang and H. Cui, “Synthesis and Characterization of Functionalized Ionic Liquid-Stabilized Metal (Gold and Platinum) Nanoparticles and Metal Nanoparticle/Carbon Nanotube Hybrids”, *Langmuir*, **2009**, 25, 2604-2612.

[16] http://neorain.com.ne.kr/study/carbon_black.pdf

[17] J. Grodkowski and P. Neta, “Reaction Kinetics in the Ionic Liquid Methyltributylammonium Bis(Trifluoromethylsulfonyl)imide. Pulse Radiolysis Study of CF3 Radical Reactions”, *J. Phys. Chem. A*, **2002**, 106, 5468-5473.

[18] C. D. Wagner, W. M. Riggs, L. E. Davis, J. F. Moulder and G. E. Muilenberg, Handbook of X-ray photoelectron spectroscopy, 1979, Perkin-Elmer Corporation, Minnesota.

[19] http://www.sigmaaldrich.com

[20] L. Li, G. Wu and B.-Q. Xu, “Electro-catalytic oxidation of CO on Pt catalyst supported on carbon nanotubes pretreated with oxidative acids”, *Carbon*, **2006**, 44, 2973–2983.

[21] F. J. Perez-Alonso, D. N. McCarthy, A. Nierhoff, P. Hernandez-Fernandez, C. Strebel, I. E. L. Stephens, J. H. Nielsen and I. Chorkendorff, “The effect of size on the oxygen electroreduction activity of mass-selected platinum nanoparticles”, *Angew. Chem. Int. Ed.*, **2012**, 51, 4641-4643.

[22] V. R. Stamenkovic, B. Fowler, B. S. Mun, G. Wang, P. N. Ross, C. A. Lucas and N. M. Markovic, “Improved oxygen reduction activity on

$Pt_3Ni(111)$ via increased surface site availability", *Science*, **2007**, 315, 493-497.

[23] K.-W. Park, J.-H. Choi, B.-K. Kwon, S.-A. Lee and Y.-E. Sung, "Chemical and Electronic Effects of Ni in Pt/Ni and Pt/Ru/Ni Alloy Nanoparticles in Methanol Electrooxidation", *J. Phys. Chem. B*, **2002**, 106, 1869-1877.

[24] D. F. van der Vliet, C. Wang, D. Li, A. P. Paulikas, J. Greeley, R. B. Rankin, D. Strmcnik, D. Tripkovic, N. M. Markovic and V. R. Stamenkovic, "Unique Electrochemical Adsorption Properties of Pt-Skin Surfaces", *Angew. Chem. Int. Ed.,* **2012**, 51, 3139 –3142.

[25] J. J. Rehr and R. C. Albers, "Scattering-matrix formulation of curved-wave multiple-scattering theory: Application to x-ray-absorption fine structure", *Phys. Rev. B*, **1990**, 41, 8139-8149.

[26] F. H. B. Lima, J. R. C. Salgado, E. R. Gonzalez and E. A. Ticianelli, "Electrocatalytic Properties of PtCo／C and PtNi／C alloys for the Oxygen Reduction Reaction in Alkaline Solution", *J. Electrochem. Soc.*, **2007**, 154, A369-A375.

[27] S. C. Zignani, E. Antolini and E. R. Gonzalez, "Stability of Pt–Ni/C (1:1) and Pt/C electrocatalysts as cathode materials for polymer electrolyte fuel cells: Effect of ageing tests", *J. Power Sources*, **2009**, 191, 344-350.

[28] N. Jung, Y.-H. Chung, D. Y. Chung, K.-H. Choi, H.-Y. Park, J. Ryu, S.-Y. Lee, M. Kim, Y.-E. Sung and S. J. Yoo, "Chemical tuning of

electrochemical properties of Pt-skin surfaces for highly active oxygen reduction reactions", *Phys. Chem. Chem. Phys.*, **2013**, 15, 17079-17083.

[29] M. Wakisaka, S. Mitsui, Y. Hirose, K. Kawashima, H. Uchida and M. Watanabe, "Electronic Structures of Pt-Co and Pt-Ru Alloys for CO-Tolerant Anode Catalysts in Polymer Electrolyte Fuel Cells Studied by EC-XPS", *J. Phys. Chem. B*, **2006**, 110, 23489-23496.

[30] L.-M. Sai and X. Y. Kong, "Microwave-assisted synthesis of water-dispersed CdTe/CdSe core/shell type II quantum dots", *Nanoscale Research Lett.*, **2011**, 399-405.

[31] J. Greeley and M. Mavrikakis, "Surface and Subsurface Hydrogen: Adsorption Properties on Transition Metals and Near-Surface Alloys", *J. Phys. Chem. B*, **2005**, 109, 3460-3471.

[32] D. Zhao and B.-Q. Xu, "Enhancement of Pt Utilization in Electrocatalysts by Using Gold Nanoparticles". *Angew. Chem. Int. Ed.*, **2006**, 45, 4955 –4959.

[33] R. Loukrakpam, J. Luo, T. He, Y. Chen, Z. Xu, P. N. Njoki, B. N. Wanjala, B. Fang, D. Mott, J. Yin, J. Klar, B. Powell and C.-J. Zhong, "Nanoengineered PtCo and PtNi Catalysts for Oxygen Reduction Reaction: An Assessment of the Structural and Electrocatalytic Properties", *J. Phys. Chem. C*, **2011**, 115, 1682–1694.

[34] X. Lu and C. Zhao, "Highly efficient and robust oxygen evolution catalysts achieved by anchoring nanocrystalline cobalt oxides onto midly oxidized multiwalled carbon nanotubes", *J. Mater. Chem. A*, **2013**, 1,

12053-12059.

[35] J.S. Yin and Z.L. Wang, “Preparation of self-assembled cobalt nanocrystal arrays”, *NanoStruct. Mater.,* **1999**, 11, 845–852.

[36] X. Sun, D. Li, Y. Ding, W. Zhu, S. Guo, Z. L. Wang and S. Sun, “Core/Shell Au/CuPt Nanoparticles and Their Dual Electrocatalysis for Both Reduction and Oxidation Reactions”, *J. Am. Chem. Soc.*, **2014**, 136, 5745−5749.

[37] Y. Liang, Y. Li, H. Wang, J. Zhou, J. Wang, T. Regier and H. Dai, “Co_3O_4 nanocrystals on graphene as a synergistic catalyst for oxygen reduction reaction”, *Nat. Mater.,* **2011**, 10, 780-786.

[38] C. Sun, F. Li, C. Ma, Y. Wang, Y. Ren, W. Yang, Z. Ma, J. Li, Y. Chen, Y. Kim and L. Chen, “Grpahene-Co_3O_4 nanocomposite as an efficient bifunctional catalyst for lithium-air batteries”, *J. Mater. Chem. A,* **2014**, 2, 7188-7196.

[39] Y. Lee, J. Suntivich, K. J. May, E. E. Perry and Y. Shao-Horn, “Synthesis and Activities of Rutile IrO_2 and RuO_2 Nanoparticles for Oxygen Evolution in Acid and Alkaline Solutions”, *J. Phys. Chem. Lett.*, **2012**, 3, 399-404.

[40] F. Svegl, B. Orel, I. Grabec-Svegl and V. Kaucic, “Characterization of spinel Co_3O_4 and Li-doped Co3O4 thin film electrocatalysts prepared by the sol–gel route”, *Electrochim. Acta*, **2000**, 45, 4359–4371.

Chapter 4. Conclusions

This study purpose the synthesis of supported nanoparticles via sputtering technique and their electrochemical applications. Sputtering technique is applied to supported nanoparticle synthesis for the first time and promising results were derived.

Carbon support dispersed non volatile liquids were applied as solvent for supported nanoparticle synthesis via sputtering and direct sputtering onto liquid leads to successful synthesis. Various ionic liquids and PEG was used as non volatile liquids, but their supporting was not equal. In case of ionic liquids, chemical bond formation between carbon support and metal surface adsorbed ions was required, since ions are strongly adsorbed on metal surface; vacuum annealing was able to induce the chemical bonding. Choice of the ionic liquid could be a important variable for supported nanoparticle synthesis, since some ions in ionic liquid are interfere bonding formation by blocking carbon surface. Whereas metal nanoparticles in PEG solvent are not strongly interact with solvent, so particles are directly supported on carbon supports by van der Waals force.

Since surfaced adsorbed ions reduce electrochemical active area and performance degradation, catalyst synthesis and activity evaluation was carried out with PEG solvent. Evenly dispersed uniform sized nanoparticles were detected by HRTEM analysis, so it can be concluded that this method is suitable for nanocatalyst synthesis.

Platinum and cobalt nanoparticles were fabricated and applied as fuel cell catalyst. ORR activity of platinum catalyst evaluated in acid media, and cobalt catalyst was applied in alkaline media after oxidized to cobalt oxide. Both catalyst showed good performances and possibility of practical application was confirmed.

PtCo/C and PtNi/C catalysts were prepared by co-sputtering, and XRD and STEM EDS analysis revealed alloy nanoparticle formation. Altered electronic structure and reduced atomic distance were detected using XRD, XAFS and XPS. Enhanced ORR activity was obtained due to above reasons and particularly PtNi/C had 2-fold catalytic activity than sing component Pt/C catalyst.

Core-shell structured nanoparticles were synthesized by microwave assisted two step liquid sputtering method. Core material was fabricated using normal liquid sputtering method and shell was deposited by microwave irradiation. Although synthesized particle has just average diameter of 2-3 nm, core-shell structure was formed. Synthesized particles exhibited superior catalytic activity due to electron transfer effect and lattice strain of core material.

Consequently, supported nanoparticles were easily synthesized via facile sputtering method, and achieved further enhanced catalytic activities.

국문초록

탄소 담지체 위에 고르게 분산된 백금 나노 입자는 다양한 전기화학 반응의 촉매로 사용되고 있는 유용한 물질이다. 백금은 대부분의 전기화학 반응에서 높은 교환 전류밀도 가지고 있어 촉매의 활성이 뛰어나며, 나노 크기의 물질로 합성할 경우 표면적 대 부피비가 급격히 증가하여 높은 전기화학적 성능을 기대할 수 있게 된다. 뿐만 아니라 탄소 담지체는 금속 나노 입자의 안정성을 높여주고 탄소에서 백금으로의 전자 전달로 인한 촉매 활성 증가 역시 기대할 수 있다.

이러한 나노 담지 백금 입자는 주로 백금 전구체를 환원시켜 입자를 형성하는 케미컬 메소드를 통해 합성되어 왔다. 그러나, 이 환원 합성법은 전구체의 높은 가격 및 실험 과정에서 사용되는 환원제와 계면활성제로 인한 환경 문제 등 경제·환경적인 측면에서 단점을 가지고 있다. 또한 전구체와 환원제의 환원 전위에 강하게 영향을 받기 때문에 원하는 조성 및 형태의 입자를 합성하는 데에도 한계가 존재한다.

본 논문에서는 금속 전구체 및 환원제, 계면활성제의 사용을 최소화하여 나노 담지 백금 입자를 합성할 수 있는 새로운 합성법을 개발하고, 합성된 입자를 전기화학적 촉매로 적용할 수 있는 방법을 고안해 보고자 한다. 전기화학적 촉매 적용 여부는 산소 환원 반응을 이용하여 평가하였다.

탄소 담지체 위에 고르게 분산된 백금 나노입자를 합성하기 위한 방법으로 이온성 액체 기판 위에 스퍼터링 하는 방법을 선정하였다. 탄소 담지체가 분산된 이온성 액체 위에 직접 백금을

스퍼터링 한 후 후 열처리를 통해 백금 입자와 탄소 담지체 사이의 결합을 강화시켜 주는 방법을 통해 나노 답지 백금 입자를 손쉽게 합성할 수 있었다. 또한 담지 메커니즘은 금속 입자 표면에 흡착된 음이온이 탄소 담지체와 직접 반응하기 때문임을 밝혀내었다. 그러나 이렇게 합성된 입자는 음이온의 강한 흡착으로 인해 백금의 표면이 전해질에 노출 되지 않아 전기화학적 촉매로 사용하기에는 적합하지 않았다.

비휘발성 고분자 물질인 PEG를 대체 기판으로 적용하여 백금 담지 촉매를 합성하였다. 이 경우 이온성 액체와 달리 후 열처리 없이도 바로 담지 입자가 합성되었으며, 이렇게 합성된 촉매는 전기화학적으로도 높은 활성을 띄는 것으로 확인 되어 액체 기판 스퍼터링이 담지 나노 촉매를 합성하는 매우 효율적인 방법임을 증명하였다.

이러한 합성법으로 백금 단일 촉매를 합성하는 데에만 그치지 않고, 다양한 구조의 촉매를 합성하는 방법으로 응용하고자 합성법의 개선을 시도하였다.

두 개 이상의 타겟을 동시에 스퍼터링 하는 코스퍼터링을 통해 백금-코발트 및 백금-니켈 합금 나노 입자를 합성하였다. XRD 및 STEM EDS 분석을 통해 단순한 코스퍼터링을 통해 합금 구조가 성공적으로 형성되었음을 알 수 있었으며 합금 촉매는 전자 구조 및 원자간 거리의 변화로 인해 개선된 성능을 보임을 확인하였다.

또한 마이크로웨이브 장비의 도움을 받아 코어-쉘 구조를 갖는 나노입자를 합성하였다. 스퍼터링을 이용하여 코어가 되는 코발트 나노입자를 비휘발성 용액 내에 합성하였고, 백금 쉘 물질의 전구체를 주입한 후 마이크로 웨이브를 조사하여 백금 쉘을

증착시켰다. 두 단계로 합성된 나노 구조는 다양한 분석 방법을 통해 2-3 nm의 매우 작은 크기에도 불구하고 코어-쉘 구조를 띄고 있음을 확인하였다. 원자의 크기가 작은 코어에 원자 간 거리 감소 및 전자 구조 변화 역시 확인하였으며, 단일 물질 촉매에 비해 높은 전기화학적 활성을 보였다.

백금 기반의 입자뿐 아니라, 자성을 띄는 코발트 옥사이드 나노 입자 역시 합성이 가능했다. 탄소 담지체를 나노 입자 합성이 끝난 후 주입하는 방식을 통해 자성을 띄는 코발트임에도 뭉침 없이 고르게 분산된 담지 입자를 합성할 수 있었으며, 이렇게 합성된 촉매는 산소 환원 반응 및 산소 생성 반응 모두에 좋은 활성을 보여 양방향 기능성 촉매로 적용 가능함을 확인했다.

본 연구를 통해 단순한 스퍼터링을 통해 고른 크기를 갖는 나노 담지 촉매를 합성할 수 있음을 보였고, 촉매 합성 과정에서 발생하는 담지 메커니즘 역시 최초로 밝혔다. 또한 합성 방법을 개선하여 백금 기반 합금 및 코어-쉘 구조의 나노 입자와 자성 산화물 나노입자 합성에도 성공하였으며, 이들 촉매는 개선된 산소 환원 성능을 보임을 알 수 있었다.

주요어: 스퍼터링, 이온성 액체, PEG, 나노 담지 촉매, 산소 환원 반응

학 번: 2009-21029